

# Feeding the fire: tracing the mass-loading of $10^7$ K galactic outflows with O VI absorption

J. Chisholm,<sup>1★</sup> R. Bordoloi,<sup>2†</sup> J. R. Rigby<sup>3</sup> and M. Bayliss<sup>2</sup>

<sup>1</sup>*Observatoire de Genève, Université de Genève, 51 Ch. des Maillettes, CH-1290 Versoix, Switzerland*

<sup>2</sup>*MIT Kavli Institute for Astrophysics and Space Research, 77 Massachusetts Ave., Cambridge, MA 02139, USA*

<sup>3</sup>*Observational Cosmology Lab, NASA Goddard Space Flight Center, 8800 Greenbelt Rd., Greenbelt, MD 20771, USA*

Accepted 2017 October 25. Received 2017 October 12; in original form 2017 August 3

## ABSTRACT

Galactic outflows regulate the amount of gas galaxies convert into stars. However, it is difficult to measure the mass outflows remove because they span a large range of temperatures and phases. Here, we study the rest-frame ultraviolet spectrum of a lensed galaxy at  $z \sim 2.9$  with prominent interstellar absorption lines from O I, tracing neutral gas, up to O VI, tracing transitional phase gas. The O VI profile mimics weak low-ionization profiles at low velocities, and strong saturated profiles at high velocities. These trends indicate that O VI gas is co-spatial with the low-ionization gas. Further, at velocities blueward of  $-200 \text{ km s}^{-1}$  the column density of the low-ionization outflow rapidly drops while the O VI column density rises, suggesting that O VI is created as the low-ionization gas is destroyed. Photoionization models do not reproduce the observed O VI, but adequately match the low-ionization gas, indicating that the phases have different formation mechanisms. Photoionized outflows are more massive than O VI outflows for most of the observed velocities, although the O VI mass outflow rate exceeds the photoionized outflow at velocities above the galaxy's escape velocity. Therefore, most gas capable of escaping the galaxy is in a hot outflow phase. We suggest that the O VI absorption is a temporary by-product of conduction transferring mass from the photoionized phase to an unobserved hot wind, and discuss how this mass-loading impacts the observed circum-galactic medium.

**Key words:** galaxies: evolution – galaxies: formation – galaxies: high-redshift – galaxies: ISM.

## 1 INTRODUCTION

Supernovae, stellar winds, cosmic rays and high-energy photons from high-mass stars accelerate gas out of star-forming regions as a galactic outflow (Heckman, Armus & Miley 1990; Heckman et al. 2000; Veilleux, Cecil & Bland-Hawthorn 2005). Removing gas from galaxies stops runaway star formation by controlling the amount of gas converted into stars (Larson 1974; White & Frenk 1991; Hopkins et al. 2014), which may establish the observed star formation history of the Universe (Madau, Pozzetti & Dickinson 1998; Springel & Hernquist 2003; Oppenheimer & Davé 2006).

While studies have established that outflows are ubiquitous in star-forming galaxies at all redshifts (Heckman, Armus & Miley 1990; Heckman et al. 2000; Pettini et al. 2002; Martin 2005; Rupke et al. 2005b; Veilleux et al. 2005; Weiner et al. 2009;

Bordoloi et al. 2014; Rubin et al. 2014; Heckman et al. 2015; Bordoloi et al. 2016b; Chisholm et al. 2016a), the amount of mass ejected by outflows – the mass outflow rate – is challenging to constrain. Galactic outflows are diffuse, making them difficult to observe with emission lines outside of the local universe (Westmoquette et al. 2009; Sharp & Bland-Hawthorn 2010; Arribas et al. 2014). Typically, studies use metal absorption lines to probe the gas along the line of sight, which provides kinematic and column density information. However, converting these measurements into a mass outflow rate requires assumptions about the geometry, ionization structure, and metallicity of the outflow. These assumptions add up to a factor of 10 uncertainty to most observed mass outflow rates (Murray et al. 2007; Chisholm et al. 2016a).

Most galactic outflow studies focus on warm gas at approximately  $10^4$  K because this gas phase has strong absorption and emission lines in the rest-frame ultraviolet (UV) and optical. However, galactic outflows are multiphase phenomena. Dense molecular outflows are observed in the local universe (Weiß et al. 1999; Matsushita et al. 2000; Leroy et al. 2015; Walter et al. 2017), with molecular

★ E-mail: john.chisholm@unige.ch

† Hubble Fellow.

mass outflow rates comparable to the neutral mass outflow rate, and up to 1.3 times larger than the star formation rate (Chisholm & Matsushita 2016). At the other end of the temperature range, X-ray observations of low-redshift galaxies reveal that a pervasive large-scale wind fluid, with a temperature greater than  $10^7$  K, dominates the thermal and kinetic energy of outflows (Griffiths et al. 2000; Strickland & Stevens 2000; Strickland & Heckman 2009). These molecular and hot winds may contain at least as much mass and energy as the  $10^4$  K phase; studies focusing only on warm outflows likely underestimate the total mass outflow rate.

Determining the mass outflow rate is additionally complicated by interactions between the different outflowing phases. Phase transitions convert molecular gas to atomic (Leroy et al. 2015), and photoionized gas is further ionized into the hot wind fluid (Strickland & Stevens 2000; Chisholm et al. 2016b), producing a shifting ionization structure. Consequently, a given outflow phase can dominate the mass and energy budget of an outflow at a given radius, velocity or time. Strickland & Stevens (2000) find that most of the soft X-rays from the local starburst M 82 are produced when mass transfers from cooler phases into the hotter wind. These regions are called mass-loading regions because they feed most of the mass into the hot wind fluid (Mac Low, McCray & Norman 1989; Suchkov et al. 1996; Strickland & Heckman 2009).

The hot wind can only be probed by X-ray observations, and only the nearest starbursts are bright enough to be observed in X-rays. Alternatively, the hot wind can be studied by observing gas that is temporarily created during mass-loading. With a cooling time of 1 Myr, ‘transitional’ gas is short-lived because it sits near the peak of the cooling curve ( $\sim 5 \times 10^5$  K; Spitzer 1956) and it must be observed shortly after it is created. The O VI 1032 Å doublet is one of the few observable tracers of this transitional gas.

Observations of the O VI doublet are challenging because the transition is in the rest-frame far-ultraviolet (FUV), and must be observed from space for local galaxies. Complicating the situation, the high-resolution configuration of the Cosmic Origins Spectrograph on the *Hubble Space Telescope* cannot observe the O VI doublet in local galaxies. The Far Ultraviolet Spectroscopic Explorer (FUSE) studied the O VI region in 16 galaxies, finding the O VI absorption line to have a velocity centroid that is  $30 \text{ km s}^{-1}$  more blueshifted than warm gas tracers, like C II, but with a similar maximum velocity (Heckman et al. 2001; Grimes et al. 2006, 2007, 2009). Few other studies have observed this important outflow phase, and the origin of O VI outflows is still unsettled.

In this paper, we analyse new spectroscopic observations of the O VI 1032 Å absorption line from a gravitationally lensed, high-redshift galaxy, SGAS J122651.3+215220, which is drawn from the Magellan Evolution of Galaxies Spectroscopic and Ultraviolet Reference Atlas (MEGASaURA). The moderate resolution MEGASaURA spectra provide unprecedented FUV wavelength coverage, with absorption lines spanning a factor of 17 in ionization potential, allowing for a detailed comparison of the O VI line profile to low-ionization lines. First, we summarize the data reduction (Section 2) and analysis of the absorption lines (Section 3). Then, we compare the velocity-resolved O VI line profile to the low-ionization absorption lines (Section 4). In Section 5, we model the low-ionization lines with photoionization models to determine whether photoionization models reproduce the observed O VI. Finally, we discuss: O VI formation mechanisms (Section 6.1), upper limits for the column density and the mass outflow rate of each phase (Section 6.2), and the physical picture suggested by these observations (Section 6.3). With this analysis, we explore what feeds the elusive and powerful  $10^7$  K hot wind.

## 2 MEGASaURA DATA

The spectra used in this paper are drawn from Project MEGASaURA: The Magellan Evolution of Galaxies Spectroscopic and Ultraviolet Reference Atlas (Rigby et al. 2017a). In short, some of the brightest gravitational lenses in the sky were observed with the Magellan Echellette (MagE) Spectrograph (Marshall et al. 2008) on the Magellan telescopes. The highest redshift galaxies within the MEGASaURA sample have MagE observations with rest-frame UV wavelengths between  $850 \lesssim \lambda_r \lesssim 2200$  Å, suitable to analyse the O VI absorption line. The spectra were reduced using D. Kelson’s Carnegie Python pipeline,<sup>1</sup> and were corrected for Milky Way foreground reddening using the observed extinction from Pan-STARRS and 2MASS observations (Green et al. 2015), assuming the Milky Way extinction law (Cardelli, Clayton & Mathis 1989).

In Fig. 1, we show the rest-frame spectra of the six MEGASaURA galaxies with O VI 1032 Å coverage. With the exception of J1429+1202, galaxies with  $\text{SNR} > 3$  show broad O VI 1032 Å absorption that is blueshifted from the stellar continuum, as demonstrated by the grey lines in Fig. 1. In a future paper, we will explore the outflow properties of the entire MEGASaURA spectral data set, but here we focus on a single galaxy, SGAS J122651.3+215220 (hereafter J1226+2152; Koester et al. 2010), because the high signal-to-noise ratio ( $\sim 10$  at 1032 Å) allows us to clearly define and characterize the O VI line profile. J1226+2152 has a redshift of  $2.926 \pm 0.0002$ , as measured from the [C III] 1907 Å and [C III] 1909 Å nebular emission doublet (Rigby et al. 2017a). The total integration time for J1226+2152 was 12.42 h, spread over multiple observing runs, with a final spectral resolution, as measured from night sky emission lines, of  $R = 4010 \pm 170$  ( $75 \pm 3 \text{ km s}^{-1}$ ). The median signal-to-noise ratio per resolution element was  $\text{SNR} = 20$ .

## 3 SPECTRAL ANALYSIS

### 3.1 Continuum fitting

The spectrum of J1226+2152 is observed ‘down-the-barrel’ such that the interstellar medium (ISM) absorption lines are imprinted on to the stellar continuum. In this subsection, we discuss how we fit and remove the stellar continuum to account for the shape and absorption lines of the background stars. We fit the stellar continuum twice: once for wavelengths greater than 1240 Å, and once for wavelengths around the O VI doublet (1015–1045 Å). The continuum must be fit twice because there are numerous intervening absorbers in the Ly $\alpha$  forest which can drive the stellar continuum fits if they are not properly masked.

Following Chisholm et al. (2015), we fit the stellar continuum redward of 1240 Å using MPFIT (Markwardt 2009) with a linear combination of 10 single-age (with ages between 1 and 40 Myr), fully theoretical STARBURST99 models (Leitherer et al. 1999, 2010) that use the Geneva stellar evolution models with high mass loss rates (Meynet et al. 1994), while simultaneously fitting for the stellar continuum extinction ( $E_s(B - V)$ ) using a Calzetti extinction law (Calzetti et al. 2000). We allow for the five STARBURST99 stellar continuum metallicities (0.05, 0.2, 0.4, 1.0,  $2.0 Z_\odot$ ), and choose the best-fitting model using a  $\chi^2$  test. The best-fitting model is overplotted on the observed data in Fig. 2 and has an  $E_s(B - V)$  of  $0.15 \pm 0.002$  mag, a stellar metallicity of  $0.2 Z_\odot$  and a light-weighted age of 11 Myr. We cross-correlate the best-fitting model

<sup>1</sup> The pipeline can be found at <http://code.obs.carnegiescience.edu/mage-pipeline>.

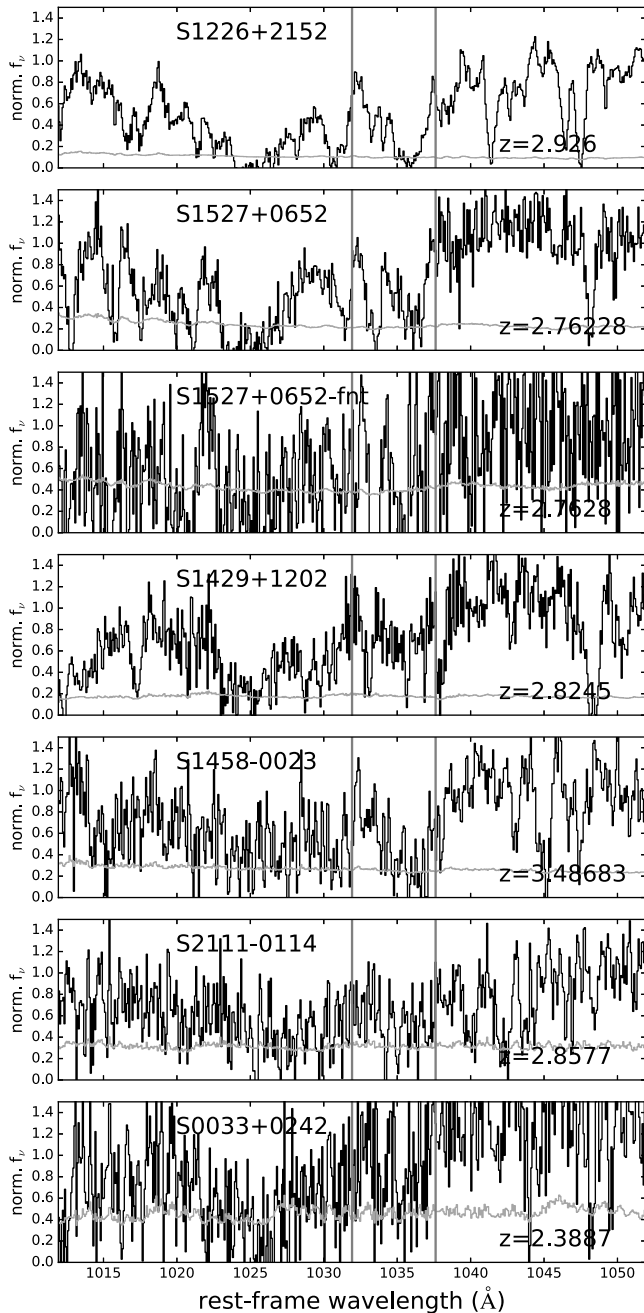


**Figure 1.** The O VI 1032 Å region for six galaxies from the MEGASaura sample, arranged in descending order of their signal-to-noise ratio at the O VI 1032 Å line, except for J1527+0652-fnt which is a fainter knot from J1527+0652. The O VI 1032 Å and 1038 Å lines are both marked by grey vertical lines. O VI 1032 Å absorption is found in three of the four highest signal-to-noise observations (J1226+2152, J1527+0652 and J1458-0023).

with the data to determine the velocity offset between the observed stellar continuum and the *STARBURST99* models. This velocity offset defines the zero-velocity of the spectrum, also known as the systemic redshift. Further, we use the fitted *STARBURST99* model as the ionizing source for the *CLOUDY* models in Section 5.2.

The O VI doublet, at wavelengths of 1032 Å and 1038 Å, is in an extremely complicated spectral region. O VI in the atmosphere of hot massive stars produces strong P-Cygni profiles (Leitherer et al. 1999), while there is strong Lyβ 1026 Å absorption from

both the background stars and the foreground ISM. Additionally, there are many strong interstellar metal absorption lines, such as Si II 1020 Å, O I 1025 Å, C II 1036 Å and O I 1039 Å, which blend with the O VI profiles. Determining the continuum in this region is challenging, but without a physically motivated continuum the broad Lyβ or stellar O VI P-Cygni profiles may be mistaken for high-velocity O VI (see Fig. 3).

We fit the O VI continuum region of J1226+2152 using a simultaneous model of empirical *STARBURST99* models and a Lyβ Voigt profile. We mask, by hand, regions of possible intervening absorbers (grey regions in Fig. 3) and interstellar metal lines. For simplicity, and because the Calzetti law is not defined at these wavelengths, we do not account for reddening. The resultant fit is shown by the red line in Fig. 3, where the zero-velocity of the O VI doublet is marked by two vertical dashed lines. The weaker O VI 1038 Å line is severely blended by the interstellar C II 1036 Å and O I 1039 Å absorption lines; we cannot use the O VI 1038 Å line for this reason.

### 3.2 Comparing the O VI absorption profile to low-ionization profiles

The stellar continuum-normalized O VI 1032 Å line profile is shown in all panels of Fig. 4 as the black line, with low-ionization lines overplotted in colours. The O VI 1032 Å line is broad (full width at half-maximum of 150 km s<sup>-1</sup>) and blueshifted relative to the stellar continuum by an average of -246 km s<sup>-1</sup>, with deep absorption at blue velocities.

In Fig. 4, we show transitions of varying strength and ionization potential. The covering fraction and optical depth govern the line profiles, and we use the equivalent width ratios of doublet absorption lines to demonstrate whether a transition is optically thick. If the weaker line in a doublet is optically thin then the ratio of the two equivalent widths will be equal to the ratio of the two transition's  $f\lambda$ , where  $f$  is the  $f$ -value of the line. Meanwhile, if the line is optically thick, the ratio of the two equivalent widths will be 1. The equivalent width ratio between Si IV 1393 Å and Si IV 1402 Å is 1.6, implying that the Si IV line is not strongly saturated because the  $f\lambda$  ratio is 2.0. Similarly, in Fig. 5 we show the Si II 1808 Å, 1527 Å and 1260 Å transitions which have  $f$ -values of 0.0025, 0.13 and 1.2, respectively. The Si II 1260 Å transition is saturated over the entire profile, while the Si II 1808 Å profile is only marginally detected ( $3\sigma$ ). The Si II 1527 Å line resides between these two extremes.

Singlets, like O I 1302 Å and Al II 1670 Å, cannot have their saturation levels diagnosed, but Fig. 4 shows that these lines have similar profiles to Si IV 1393 Å. Meanwhile, lines like C II 1335 Å, Si III 1206 Å and Si II 1260 Å are nearly black at all velocities, implying that they are saturated at all velocities. Consequently, Fig. 4 shows four strong lines (Si III 1206 Å, Si II 1260 Å, C II 1335 Å and C IV 1548 Å) and four relatively weak lines (O I 1302 Å, Si IV 1393 Å, Al II 1670 Å and Al III 1863 Å).

By visual inspection of Fig. 4, we compare the O VI and low-ionization line profiles. The shape and depth of the velocity profiles are insensitive to the ionization potential of the line: the Si II 1260 Å profile has a lower ionization potential than the Si IV 1393 Å line, but the Si II profile extends to larger velocities. At velocities between +100 and -200 km s<sup>-1</sup>, the shape and depth of the O VI profile resemble those of the weak lines like O I 1302 Å, Al II 1670 Å, Al III 1863 Å and Si IV 1393 Å; while at velocities blueward of -200 km s<sup>-1</sup>, the O VI profile resembles the strong Si II 1260 Å and C II 1335 Å lines. Consequently, the O VI profile has two regimes: a low-velocity regime that follows the weak lines, and a high-velocity regime that follows the saturated lines. This indicates

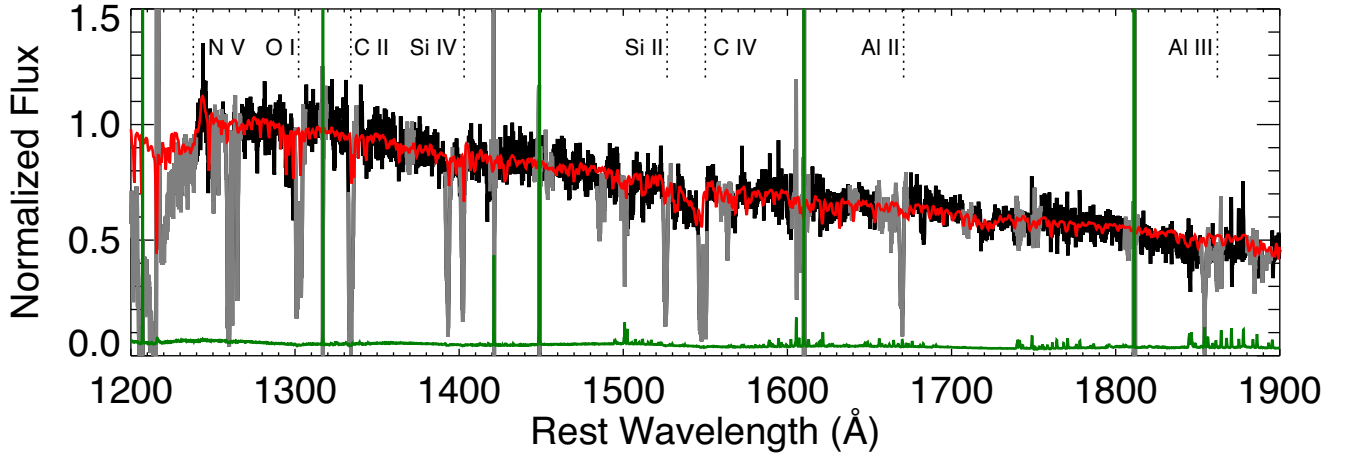


**Figure 2.** Observed spectrum (in  $F_\lambda$ ) of J1226+2152 in black for the rest-frame wavelength regime between 1200 and 1900 Å, with the error array included in dark green. Grey areas are masked out of the stellar continuum fitting to avoid interstellar and intervening absorption lines. Overplotted in red is the STARBURST99 stellar continuum fit to the data (see Section 3.1). The stellar continuum fit establishes the continuum level and the zero-velocity (systematic) of the spectrum. The best-fitting stellar continuum model has a light-weighted age of 11 Myr, a stellar metallicity of  $0.2 Z_\odot$ , and stellar extinction of  $E(B - V) = 0.15$  mag. Interstellar absorption lines used in the paper are marked by dashed lines in the upper portion of the plot.

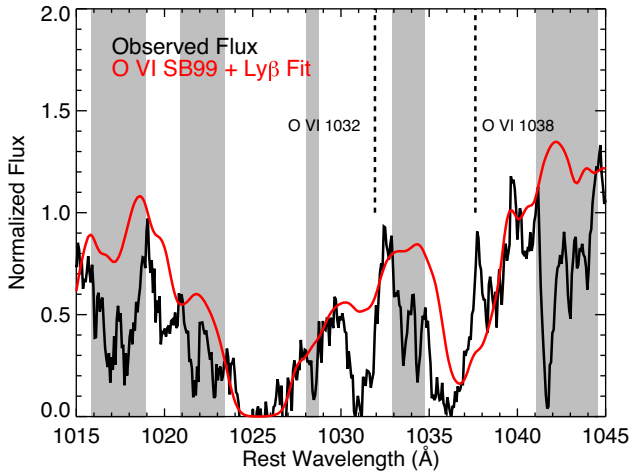


**Figure 3.** The simultaneous STARBURST99 and Ly $\beta$  fit (red line) to the O VI region (black line) for the lensed galaxy J1226+2152. The zero-velocity, as determined by the redshift from the stellar continuum fitting, of the O VI 1032 Å and 1038 Å lines is denoted by dashed vertical lines. The O VI 1038 Å line is heavily blended by nearby interstellar O I and C II lines, and we do not use that line in our analysis. The STARBURST99 fit accounts for the stellar continuum and Ly $\beta$  contributions to establish the unity flux level of the O VI profile below. Grey regions show areas of intervening absorbers that were masked from the continuum fit.

that the O VI profile is sensitive to the optical depth at low velocities, but it is saturated at high velocities. We return to this in Section 4.

### 3.3 Velocity-resolved apparent optical depth profiles

The strength of a line is approximated by the optical depth ( $\tau$ ), a proxy for the column density. The apparent optical depth ( $\tau_{\text{AOD}}$ ; Savage & Sembach 1991) gives a lower limit of  $\tau$  because the covering fraction ( $C_f$ ), resolution effects and saturation can increase the actual  $\tau$  (see Section 4). In the upper panel of Fig. 6, we explore how the  $\tau_{\text{AOD}}$  of four ions evolves with velocity. The saturated C II 1334 Å and Si II 1260 Å distributions are similar, while the Al II 1670 Å distribution is a factor of 2.3 smaller. The Al II  $\tau_{\text{AOD}}$  does

not rise much above 1, while C II and Si II are above two for all velocities between 0 and  $-350$  km s $^{-1}$ , and decline collectively at bluer velocities.

The O VI 1032 Å  $\tau_{\text{AOD}}$  follows the Al II  $\tau_{\text{AOD}}$  from 0 to  $-200$  km s $^{-1}$ , and rapidly increases at bluer velocities. At the highest velocities, the O VI profile declines on the same trajectory as the C II and Si II profiles. The velocity-resolved  $\tau_{\text{AOD}}$  follows the two-regime scenario for the O VI profile outlined above.

The two-regime behaviour is emphasized when we sum the  $\tau_{\text{AOD}}$  with velocity (lower panel of Fig. 6). Again, the O VI  $\tau_{\text{AOD}}$  rapidly diverges from the Al II profile at velocities blueward of  $-200$  km s $^{-1}$  (marked by the vertical dashed line), and approaches the C II and Si II distributions. At  $-200$  km s $^{-1}$ , the O VI profile shifts from behaving as a weak line (like Al II 1670 Å) to behaving as a strong line (like C II 1335 Å or Si II 1260 Å). In Section 4, we use the weak Si IV doublet to explore a possible physical mechanism for these two regimes.

The similarity between the O VI and low-ionization line profiles indicates that the different ions are comoving because they have similar absorption at similar velocities. Moreover, it appears that the O VI transition strengthens at velocities blueward of  $-200$  km s $^{-1}$ , and the profile declines in tandem with the strongest transitions at the bluest velocities. Since these lines all have different optical depths, the shared decline at high velocities is likely due to a declining covering fraction. The covering fraction relates the physical sizes of the outflow, consequently, the similar covering fractions indicate that the O VI is also co-spatial with low-ionization gas.

### 3.4 Velocities of photoionized and transitional gas

We measure the velocities for each transition in two ways (Table 1). The first way is the central velocity ( $v_{\text{cen}}$ ), which is defined as the velocity at half of the total equivalent width of the line.  $v_{\text{cen}}$  is influenced by zero-velocity absorption (Chisholm et al. 2015), or by resonance emission lines (Prochaska, Kasen & Rubin 2011a; Scarlata & Panagia 2015), therefore we also measure the velocity at which the line profile reaches 90 percent of the continuum on the blue-side of the profile ( $v_{90}$ ). We estimate the errors on each quantity by producing 1000 realizations of the data by multiplying



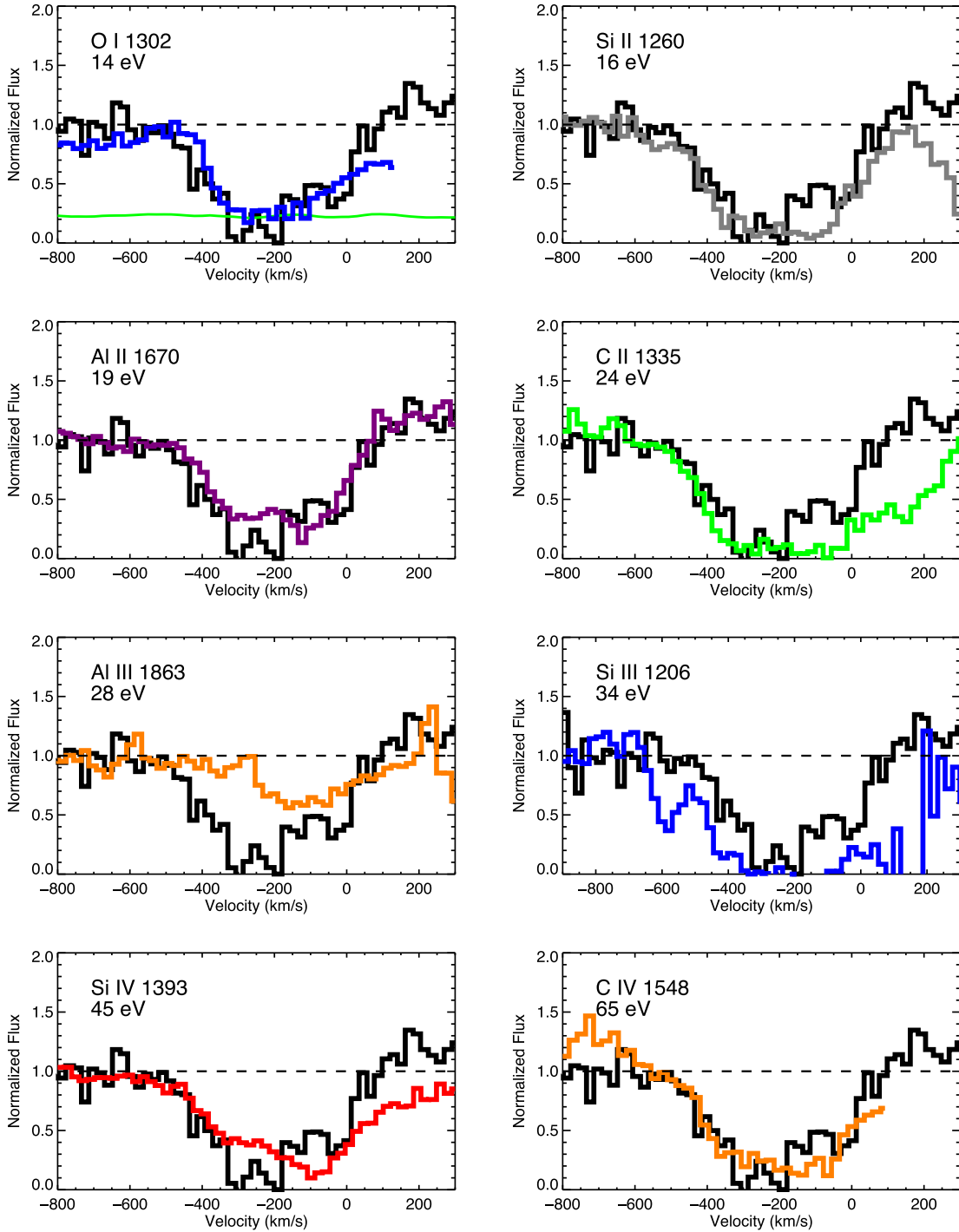


**Figure 4.** Comparison of the stellar continuum-normalized absorption profiles for various ISM metal absorption lines (in colours) with the O VI line profile in black in all the panels. The panels are ordered in terms of increasing ionization potential of the low-ionization transition. O I 1302 Å, Al II 1670 Å, Al III 1863 Å and Si IV 1393 Å are not black at any portion of their line profiles, and are considered weak lines. Conversely, the Si II 1260 Å, Si III 1206 Å and C II 1335 Å lines are nearly black over 400 km s<sup>-1</sup>, and are considered strong lines. Note that the Si III 1206 Å line is close to the broad Lyα absorption line, and we fit a spline to further normalize the spectrum. The error array corresponding to the O VI region is shown in green in the top left panel (the O I panel). Blueward of -200 km s<sup>-1</sup>, the O VI profile is similar to the strong low-ionization absorption lines – like Si II, Si III and C II – while the depth and shape of the O VI profile redward of -200 km s<sup>-1</sup> are similar to the weak lines – like Al II, Al III and O I.

each observed pixel by a random number drawn from a Gaussian distribution centred on zero with a standard deviation equal to the error on the flux.

The velocities of the individual transitions confirm what we saw by eye in Fig. 4: strong transitions (Si II 1260 Å, Si III 1206 Å and

C II 1334 Å) have large  $v_{90}$ , while weaker transitions (Al II 1670 and Si IV 1402 Å) have significantly smaller  $v_{90}$ . Since O VI follows the weaker lines at low velocity and the stronger lines at high velocity, the  $v_{\text{cen}}$  – which is weighted by the equivalent width – shifts bluewards. Therefore, O VI has the largest  $v_{\text{cen}}$  of any transition, even

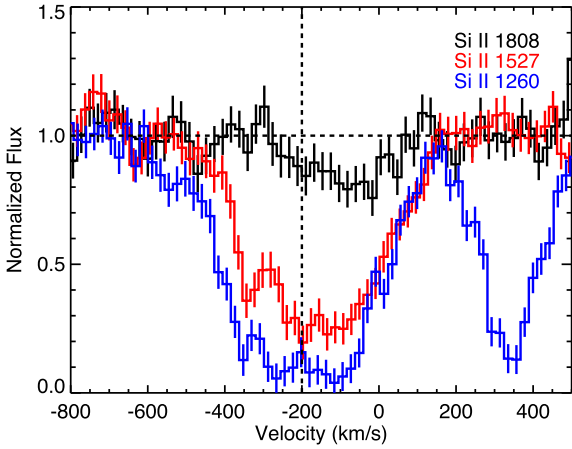


**Figure 5.** The Si II 1808 Å (black), Si II 1527 Å (red) and Si II 1260 Å (blue) absorption profiles. The error bars show the  $1\sigma$  flux errors. The Si II absorption lines have  $f$ -values of 0.0025, 0.13 and 1.22, respectively. There is an intervening absorber (detected with a doublet finding algorithm) at  $+350 \text{ km s}^{-1}$  from the Si II 1260 Å line. The marginal detection ( $3\sigma$ ) of Si II 1808 Å leads to a Si II column density of  $\log(N[\text{cm}^{-2}]) = 15.57 \pm 0.14$ , consistent, within  $2\sigma$ , with the Si II column densities measured from the Si II 1527 Å line. The weak Si II 1808 Å line is not significantly detected blueward of  $-200 \text{ km s}^{-1}$  (vertical dashed line), which is the velocity where the photoionized density begins to rapidly decline (see Section 4.2).

though other transitions have larger (Si II, Si III), or comparable (C II),  $v_{90}$ . The two-regime behaviour of O VI may explain why previous studies, which only quantized the outflow velocity with  $v_{\text{cen}}$ , found a larger  $v_{\text{cen}}$  for O VI than the low-ionization lines, even though the O VI absorption profiles did not extend bluer than the low-ionization lines (fig. 3 of Heckman et al. 2001; Grimes et al. 2009).

### 3.5 The non-detection of N V

Before proceeding, one notable exception to these observations is the N V 1243 Å line (see Fig. 7). Strangely, interstellar N V 1243 Å is not detected in absorption in the spectrum of J1226+2152, even though N V has an ionization potential between the observed O VI and C IV transitions. N V 1243 Å is a relatively strong transition ( $f$ -value of 0.08) arising from a cosmologically abundant element ( $N/H = 7.5 \times 10^{-5}$ ; Jenkins 2009), indicating that there is negligible gas in the N V ionization state. N V is also rarely detected in lower redshift galactic outflows (Chisholm et al. 2016a), providing a clue about the ionization structure of galactic outflows. We will use the N V non-detection in Section 6.1 when we explore how O VI is produced.

## 4 MODELLING THE ABSORPTION LINE PROFILES

In the previous section, we found that the O VI line profile has two regimes bisected at  $-200 \text{ km s}^{-1}$ : the depth of the O VI line matches the weak lines at redder velocities, while the depth matches the strong lines at bluer velocities. Here, we model the line profiles to explore the origin of this two-regime behaviour.

### 4.1 Velocity-resolved optical depths and covering fractions

There are two degenerate ways to change the depth of an absorption profile:  $C_f$  and  $\tau$ . Both these quantities change with velocity to

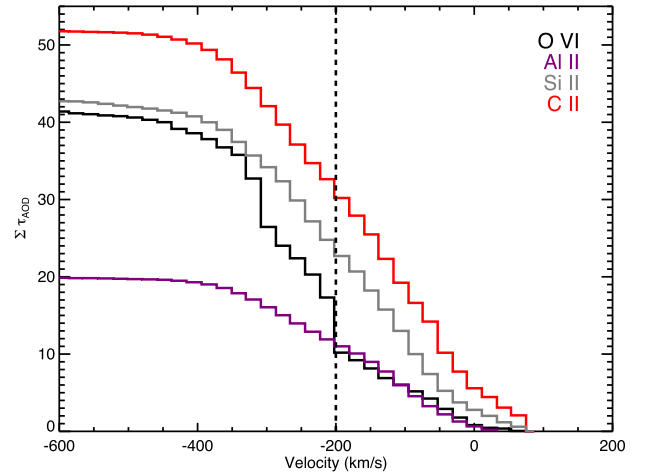
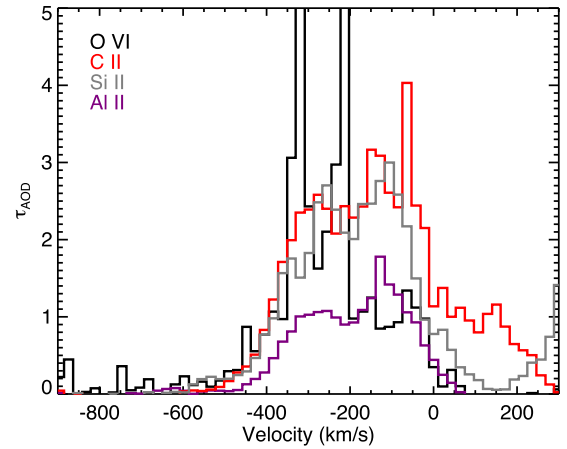


**Figure 6.** Upper Panel: Velocity-resolved apparent optical depth ( $\tau_{\text{AOD}}$ ) distributions for four transitions: O VI 1032 Å (black line), C II 1335 Å (red line), Si II 1260 Å (grey line) and Al II 1670 Å (purple line). The C II and Si II lines are saturated over the entire profile, while the Al II line is not. Lower Panel: Cumulative  $\tau_{\text{AOD}}$  distribution summed from positive velocities to negative velocities for the same ions as the upper panel. The O VI  $\Sigma \tau_{\text{AOD}}$  matches the Al II  $\Sigma \tau_{\text{AOD}}$  from 0 to  $-200 \text{ km s}^{-1}$  (marked by the dashed vertical line), while it matches the Si II and C II distributions at velocities blueward of  $-200 \text{ km s}^{-1}$ .

produce the observed profile.  $C_f$  is the fraction of the total area of the background continuum source that the absorbing gas covers. A  $C_f$  of 1 means that the gas completely covers the background stellar continuum, while a  $C_f$  of 0 means that the gas does not cover the background source. If  $\tau$  is large, then the depth of the line is  $1 - C_f$ .

The second way to change the depth of an absorption profile is through the optical depth, or approximately the column density ( $N$ ). At  $\tau$  greater than 3, the line becomes optically thick and  $C_f$  completely sets the depth of the line. Meanwhile, at lower optical depths some light passes through the gas, and the flux is no longer zero. Consequently, the depth of an absorption line is degenerate with both  $\tau$  and  $C_f$ . The radiative transfer equation describes this degeneracy as

$$F(v) = 1 - C_f(v) + C_f(v)e^{-\tau(v)}, \quad (1)$$

where  $F(v)$  is the continuum-normalized flux transmitted through the gas at a particular velocity ( $v$ ). The only way for  $F(v)$  to approach zero is if  $C_f(v)$  approaches 1 and  $\tau(v) > 3$  ( $e^{-3} = 0.05$ ), otherwise the line has residual flux. This is seen in Figs 4 and 5 where the

**Table 1.** Quantities derived from the interstellar metal absorption lines of J1226+2152. Column 1 indicates the transition, column 2 gives the ionization potential, column 3 gives the velocity at half the equivalent width ( $v_{\text{cen}}$ ), column 4 gives the velocity at 90 per cent of the continuum on the blue portion of the profile ( $v_{90}$ ), column 5 gives the rest-frame equivalent width ( $W_r$ ), column 6 gives the measured apparent optical depth column density calculated using equation (10) ( $N$ ), and column 7 gives the column density of the best-fitting CLOUDY model. Transitions that are blended with other transitions are denoted by a ‘b’. Possibly saturated lines are marked with an ‘s’. The N v 1243 Å line is reported as an upper limit because the line is not detected (ND; see Fig. 7). Transitions used in the CLOUDY modelling are denoted with a ‘c’.

| Line           | Ionization potential<br>[eV] | $v_{\text{cen}}$<br>[km s <sup>-1</sup> ] | $v_{90}$<br>[km s <sup>-1</sup> ] | $W_r$<br>[Å]      | $\log(N)$<br>[log(cm <sup>-2</sup> )] | CLOUDY $\log(N)$<br>[log(cm <sup>-2</sup> )] |
|----------------|------------------------------|---|-----------------------------------|-------------------|---------------------------------------|--|
| (1)            | (2)                          | (3)                                       | (4)                               | (5)               | (6)                                   | (7)  |
| Si I 1845.51   | 8.2                          | $-16 \pm 117$                             | $-35 \pm 10$                      | $0.24 \pm 0.03$   | $13.28 \pm 0.13$                      | 10.82  |
| O I 1302.17    | 13.6                         | $-175 \pm 8$                              | $-429 \pm 14$                     | $1.32 \pm 0.05$   | $15.62 \pm 0.11$                      | 16.13 <sup>c</sup>                           |
| Fe II 1608.46  | 16.2                         | $-158 \pm 7$                              | $-363 \pm 36$                     | $0.64 \pm 0.06$   | $14.85 \pm 0.03$                      | 14.34  |
| Si II 1808.00  | 16.3                         | $-93 \pm 31$                              | $-168 \pm 4$                      | $0.25 \pm 0.08$   | $15.57 \pm 0.14$                      | 15.13  |
| Si II 1304.37  | 16.3                         | $-175 \pm 5^b$                            | <sup>b</sup>                      | $1.18 \pm 0.12^b$ | $15.23 \pm 0.02^b$                    | 15.13  |
| Si II 1526.71  | 16.3                         | $-162 \pm 12$                             | $-466 \pm 9$                      | $1.63 \pm 0.16$   | $15.15 \pm 0.08$                      | 15.13 <sup>c</sup>                           |
| Si II 1190.42  | 16.3                         | $-236 \pm 4^b$                            | $-631 \pm 17^b$                   | $1.91 \pm 0.19^b$ | $> 15.0^s$                            | 15.13  |
| Si II 1193.29  | 16.3                         | $-169 \pm 4$                              | $-450 \pm 17$                     | $1.50 \pm 0.15$   | $> 15.0^s$                            | 15.12  |
| Si II 1260.42  | 16.3                         | $-201 \pm 10$                             | $-585 \pm 40$                     | $1.78 \pm 0.25$   | $> 14.46^s$                           | 15.13  |
| Al II 1670.79  | 18.8                         | $-196 \pm 14$                             | $-448 \pm 8$                      | $1.51 \pm 0.15$   | $13.88 \pm 0.04$                      | 13.81 <sup>c</sup>                           |
| S II 1250.58   | 23.3                         | $-110 \pm 49$                             | $-127 \pm 7$                      | $0.24 \pm 0.03$   | $15.61 \pm 0.05$                      | 14.95  |
| C II 1334.53   | 24.4                         | $-125 \pm 8$                              | $-505 \pm 33$                     | $2.43 \pm 0.24$   | $> 15.52^s$                           | 16.37  |
| Al III 1854.72 | 28.4                         | $-109 \pm 25$                             | $-369 \pm 9$                      | $1.12 \pm 0.11$   | $14.06 \pm 0.06$                      | 14.91  |
| Al III 1862.79 | 28.4                         | $-104 \pm 31$                             | $-254 \pm 13$                     | $0.80 \pm 0.08$   | $14.15 \pm 0.04$                      | 13.91 <sup>c</sup>                           |
| Si III 1206.51 | 33.5                         | $-184 \pm 98$                             | $-650 \pm 13$                     | $2.80 \pm 0.28$   | $> 14.40^s$                           | 15.39  |
| Si IV 1393.76  | 45.1                         | $-130 \pm 9$                              | $-455 \pm 10$                     | $1.85 \pm 0.18$   | $14.68 \pm 0.03$                      | 14.78  |
| Si IV 1403.77  | 45.1                         | $-153 \pm 11$                             | $-394 \pm 15$                     | $1.15 \pm 0.12$   | $14.69 \pm 0.04$                      | 14.78 <sup>c</sup>                           |
| C IV 1548.20   | 64.5                         | $-194 \pm 55^b$                           | $-478 \pm 150$                    | <sup>s, b</sup>   | $> 15.10^{s, b}$                      | 15.60  |
| C IV 1550.77   | 64.5                         | $-146 \pm 18^b$                           | <sup>b</sup>                      | <sup>s, b</sup>   | $> 15.23^{s, b}$                      | 15.60  |
| N v 1242.80    | 97.9                         | –   | –                                 | ND                | $< 14.25$                             | 10.89  |
| O VI 1031.91   | 138                          | $-246 \pm 11$                             | $-532 \pm 2$                      | $2.46 \pm 0.25$   | $15.35 \pm 0.05^s$                    | 0  |

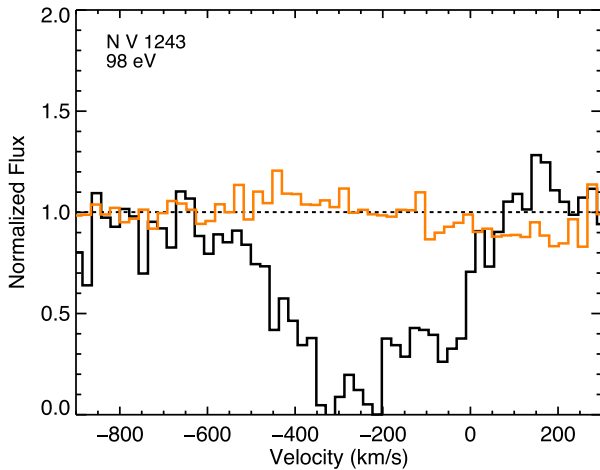


**Figure 7.** Comparison of the stellar continuum-normalized absorption profiles for the N v 1243 Å transition (orange line) and the O vi 1032 Å transition (black line). The dashed black line marks the unity flux level. The N v 1243 Å line is not detected in the spectrum, placing an upper limit on the N v column density.

weak lines (O I 1302 Å, Si II 1527 Å, Al II 1670 Å and Si IV 1393 Å) all have non-zero flux across their line profiles, while the strong lines (Si II 1260 Å and C II 1335 Å) have an average depth of 0.1 between 0 and  $-300$  km s<sup>-1</sup>, implying that  $C_f(v) \approx 0.9$ .

The degeneracy between  $C_f$  and  $\tau$  is broken with a doublet from the same ionic species. With a doublet, equation (1) becomes a system of two equations where each line has the same  $C_f$  and their  $\tau$  is related by the ratio of their  $f$ -values. The Si IV 1402 Å and Si IV

1393 Å doublet has an  $f$ -value ratio of 2. The system of equations exactly solves for  $C_f$  and  $\tau$  in terms of the flux of the two transitions as

$$C_f(v) = \frac{F_W(v)^2 - 2F_W(v) + 1}{F_S(v) - 2F_W(v) + 1}$$

$$\tau(v) = \ln \left( \frac{C_f(v)}{C_f(v) + F_W(v) - 1} \right), \quad (2)$$

where  $F_W(v)$  is the flux of the weaker doublet line at a given velocity and  $F_S(v)$  is the flux of the stronger line. We calculate the errors on  $C_f(v)$  and  $\tau(v)$  by performing a Monte Carlo analysis at each velocity, similar to how we calculated the velocity errors.

Using equation (2), we solve for the Si IV  $C_f$  and  $\tau$  at each velocity (Fig. 8). At very low velocities, the  $\tau$  and  $C_f$  are impacted by zero-velocity absorption and resonance emission (Prochaska et al. 2011a; Scarlata & Panagia 2015). To assess the contamination from the emission, we use the Si II\* 1197 Å non-resonant emission line to determine which velocities are contaminated by the emission. The Si II\* line is narrow, with emission only within  $\pm 50$  km s<sup>-1</sup>, therefore, we exclude those velocities from consideration (grey points in Fig. 8).

In the lower left panel of Fig. 8,  $C_f(v)$  declines at velocities blueward of  $-40$  km s<sup>-1</sup> until velocities near  $-300$  km s<sup>-1</sup> where it increases from  $\approx 70$  per cent covered to fully covered, and then rapidly settles to zero coverage. The increase blueward of  $-300$  km s<sup>-1</sup> in  $C_f$  is observed in the Si II 1260 Å, Si IV 1393 Å and Al II 1670 Å profiles as a ‘second component’ (Fig. 4).

The Si IV  $\tau(v)$  peaks at velocities near  $-175$  km s<sup>-1</sup>, and declines at velocities blueward of  $-200$  km s<sup>-1</sup> (upper right panel of Fig. 8). At the bluest velocities, the Si IV 1402 Å line profile is set by both

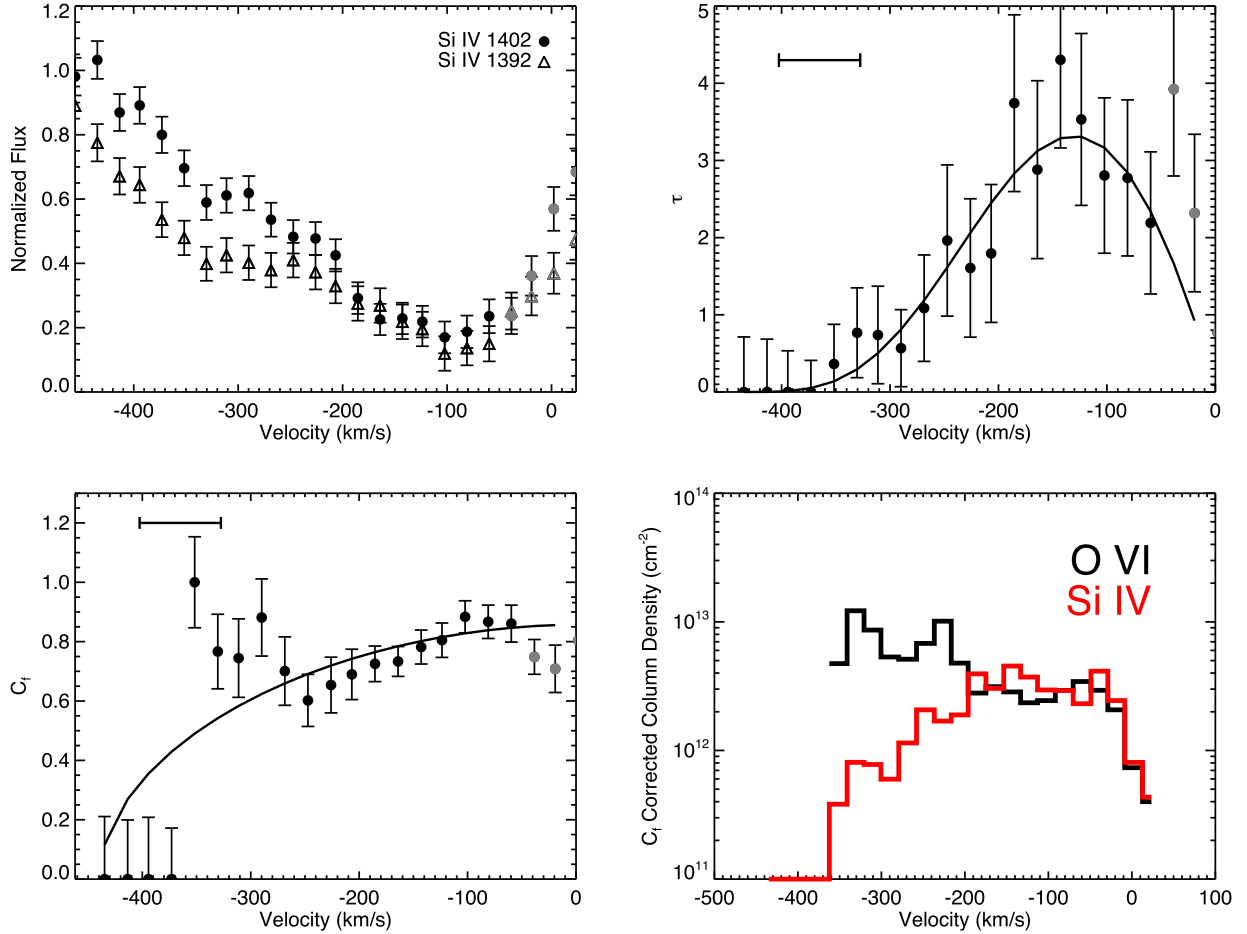


**Figure 8.** Si IV profile fits. The upper left panel shows the Si IV 1402 Å (filled circles) and Si IV 1392 Å (triangles) profiles. The grey points are excluded from the fit due to contamination with resonance emission, as determined from the Si II\* emission line. These profiles are used to calculate the velocity-resolved optical depth ( $\tau$ ; upper right panel) and covering fraction ( $C_f$ ; lower left panel) using the radiative transfer equation (equation 2). We simultaneously fit a model to the  $C_f$  and  $\tau$  distributions (equation 8) as shown by the solid lines in the two panels. In the lower right panel, we use the observed Si IV  $C_f$  to correct the O VI (black) and Si IV (red) column densities for partial coverage, assuming that O VI and Si IV have similar  $C_f$ . At velocities blueward of  $-200$  km s $^{-1}$ , the column density profiles diverge: the Si IV column density rapidly decreases while the O VI column density increases. The velocity resolution of 75 km s $^{-1}$  is indicated by bars in the  $\tau$  and  $C_f$  panels.

$C_f(v)$  and  $\tau(v)$  because  $\tau(v) < 3$ . Meanwhile, stronger lines, like C II 1335 Å and Si II 1260 Å, still have  $\tau(v) > 3$  at these velocities, and their line profiles do not change appreciably until velocities blueward of  $-350$  km s $^{-1}$  when  $C_f(v)$  rapidly drops. The degeneracy between  $\tau(v)$  and  $C_f(v)$  dominates the line profiles of weak lines, while  $C_f(v)$  determines the line profiles of strong lines.

#### 4.1.1 An origin of the two-regime behaviour of O VI

Fig. 8 illustrates why the O VI profile has two regimes. At low velocities, the O VI profile follows the  $\tau$  dominated regimes of the weak lines, while at velocities blueward of  $-200$  km s $^{-1}$  O VI is optically thick and the line profile is determined by  $C_f$ . This split at  $-200$  km s $^{-1}$  is the same velocity where the Si IV  $\tau$  begins to decline, indicating that the O VI  $\tau$  increases as the Si IV  $\tau$  decreases.

To illustrate this, we take the observed Si IV  $C_f$  from the lower left panel of Fig. 8 and correct the O VI column density for the partial coverage (bottom right panel of Fig. 8; see Section 5.1 for details on this correction). At redder velocities, the Si IV and O VI column densities follow similar trends, but at bluer velocities the Si IV column density decreases as the O VI column density increases.

The increased O VI column density means that O VI becomes a strong line, like Si II 1260 Å or C II 1335 Å, and the blue-wing of the O VI profile is now fixed by  $C_f$ . This also means that at bluer velocities the O VI line likely saturates, and the derived velocity-resolved column densities are lower limits. The transition of O VI from an optically thin line to an optically thick line naturally explains the two-regime O VI profile: at redder velocities, the O VI profile matches the weak transitions whose profiles are governed by changes in  $\tau$  at a nearly constant  $C_f$ , while at bluer velocities the O VI profile resembles the strong transitions whose profiles change as  $C_f$  changes. Similar behaviour is also observed in other high signal-to-noise ratio spectra in the MEGASaura sample (see J1527+0652 in Fig. 1).

#### 4.2 A model describing the Si IV profile

Above, we found that the O VI column density rises as the Si IV column density declines. This suggests a relationship between the two phases of gas that we discuss further in Section 6.3. To gain insight into this connection, here we explore a physical model for the Si IV profile. This model was fully introduced in Chisholm et al. (2016b), and we refer the reader there for details on its derivation.



Physically,  $C_f$  varies with velocity because the absorbing clouds cover a changing amount of the total area of the background stellar continuum. This change is caused by geometric dilution – the clouds occupy a smaller fraction of the total area at larger radii – or because the size of the outflowing clouds changes with velocity (Martin & Bouché 2009; Steidel et al. 2010). A simple geometric model relates changes in  $C_f$  to changes in the area occupied by the absorbing gas as a power law with

$$C_f(r) = C_f(R_i) \left( \frac{r}{R_i} \right)^\gamma, \quad (3)$$

where  $C_f(R_i)$  is the covering fraction at the initial radius ( $R_i$ ) and  $\gamma$  is an unknown power-law exponent. Introducing normalized coordinates simplifies this relation, such that

$$C_f(x) = C_f(R_i)x^\gamma, \quad (4)$$

where  $x = r/R_i$ . If the outflowing clouds remain the same size,  $C_f$  decreases with radius as a power of  $\gamma = -2$  as the projected area increases as  $r^2$ . For a local star-forming galaxy, NGC 6090, Chisholm et al. (2016b) find that the  $C_f$  evolves as  $r^{-0.8}$ , less rapidly (lower  $\gamma$ ) than expected from geometric dilution, but consistent with the outflow adiabatically expanding as it accelerates.

Changes in  $\tau(v)$  come from two sources: changes in the density of the absorbers ( $n(v)$ ) and the velocity distribution of the absorbers. A power law describes the radial change in density, such that

$$n(r) = n_0 \left( \frac{r}{R_i} \right)^\alpha = n_0 x^\alpha, \quad (5)$$

where  $\alpha = -2$  if the outflow is a mass-conserving spherical outflow, and  $\alpha < -2$  if gas is removed from the outflow, or if the geometry significantly deviates from a spherical outflow (Fielding et al. 2017). Possible ways to remove gas from the outflow are ionizing the outflow to a different ionization state (Chisholm et al. 2016b) or if gas exits the outflow as a galactic fountain (Leroy et al. 2015). Again for NGC 6090, Chisholm et al. (2016b) find  $\alpha = -5.7$ , possibly because a hot outflow destroys the low-ionization gas and incorporates it into a hotter outflow.

Changing how the gas is distributed in velocity also changes  $\tau(v)$ . Often times Gaussian or Lorentzian velocity distributions are assumed, where the absorbers are spread out in velocity space due to their thermal (or turbulent) motions (Rupke, Veilleux & Sanders 2005a; Martin & Bouché 2009; Chen et al. 2010). However, these assumed velocity distributions do not describe galactic outflows in which the radial velocity gradient broadens the observed line profile. The outflow velocity gradient measures how rapidly the velocity changes with radius ( $dv/dr$ ). If  $dv/dr$  is large, then the velocity of the outflow rapidly changes while only travelling a short radial distance. In this case, there are fewer total absorbers per velocity interval, and correspondingly the optical depth is lower. Conversely, a small  $dv/dr$  means that the outflow accelerates gradually with radius, piling more absorbers into each velocity interval. The Sobolev approximation (Sobolev 1960) defines  $\tau(v)$  in terms of the density and radial velocity gradient as

$$\tau(v) = \frac{\pi e^2}{mc} f \lambda_0 n(v) \frac{dr}{dv}, \quad (6)$$

where  $f$  is the  $f$ -value of the transition,  $\lambda_0$  is the transition's rest wavelength and  $m$  is the mass of the electron.

The velocity gradient is not known a priori, but we fit for it from the shape of  $\tau(v)$  and  $C_f(v)$  (Fig. 8). Analytic relations for the acceleration (or deceleration) of outflows find that the velocity

changes with radius (Murray, Quataert & Thompson 2005) as a  $\beta$ -velocity law (Lamers & Cassinelli 1999), such that

$$v = v_\infty \left( 1 - \frac{R_i}{r} \right)^\beta = v_\infty \left( 1 - \frac{1}{x} \right)^\beta, \quad (7)$$

where  $v_\infty$  is the maximum observed velocity (440 km s<sup>-1</sup> for Si IV 1402 Å). It is important to note that equation (7) does not require that the outflow accelerates: a negative  $\beta$  produces a decelerating profile. Rather, we fit for  $\beta$  from the Si IV 1402 Å profile, while allowing for  $\beta$  values between  $-5$  and  $+5$ . The shape of  $\tau(v)$  and  $C_f(v)$  defines whether the outflow is accelerating or decelerating. In Chisholm et al. (2016b), NGC 6090 has  $\beta = 0.43$ , which is consistent with a  $r^{-2}$  force law opposed by gravity, such as ram pressure.

The derivative of equation (7) defines the velocity gradient, allowing for the  $C_f$  (equation 4) and  $\tau$  (equation 6) distributions to be rewritten in terms of the normalized velocity ( $w = v/v_\infty$ ) as

$$\begin{aligned} \tau(w) &= \frac{\pi e^2}{mc} f \lambda_0 \frac{R_i}{v_\infty} n_{4,0} x^\alpha \frac{dx}{dw} = \tau_0 \frac{w^{1/\beta-1}}{\beta(1-w^{1/\beta})^{2+\alpha}} \\ C_f(w) &= \frac{C_f(R_i)}{(1-w^{1/\beta})^\gamma}, \end{aligned} \quad (8)$$

where  $n_{4,0}$  is the Si IV density at  $R_i$ . The constant preceding the  $\tau$  distribution is rewritten as

$$\tau_0 = \frac{\pi e^2}{mc} f \lambda_0 \frac{R_i}{v_\infty} n_{H,0} \chi_{Si4} (Si/H), \quad (9)$$

where  $n_{H,0}$  is the total hydrogen density at the base of the outflow,  $\chi_{Si4}$  is the Si IV ionization fraction and Si/H is the silicon-to-hydrogen abundance. With the ionization models of Section 5.2, we solve for  $R_i$  in equation (9) to derive the initial radius of the outflow.

We use MPFIT (Markwardt 2009) to fit for the five parameters in equation (8) ( $\tau_0$ ,  $C_f(R_i)$ ,  $\beta$ ,  $\alpha$ ,  $\gamma$ ; see Table 2). In Table 2, we compare the fitted parameters to the local star-forming galaxy NGC 6090 (Chisholm et al. 2016b).  $\beta$ ,  $\alpha$  and  $\gamma$  describe the radial variation of  $C_f$  (equation 4), density (equation 5) and velocity (equation 7); these exponents are similar to local galaxies. This implies that the outflow properties of high- and low-redshift galaxies vary similarly with radius (Rigby et al. 2017b). Intriguingly, the  $C_f(R_i)$  of 0.86 is roughly consistent with the maximum depth of the Si II 1260 Å and C II 1335 Å lines being near 0.1 in normalized flux units, further emphasizing that these lines are optically thick and dominated by  $C_f$ .

These models illustrate many interesting features of the Si IV profiles. For instance, the rapid acceleration ( $\beta = 0.53$ ) of the outflow means that the outflow initially does not travel a large distance in each velocity interval. This rapid acceleration means that the dynamical time, as defined by the velocity profile (equation 7), is only  $\sim 0.2$  Myr. Since the density decreases with radius, not velocity, the rapid acceleration ensures that the density does not decrease appreciably in each redder velocity interval. In fact, equation (5) implies that at  $-200$  km s<sup>-1</sup> the density is still 20 per cent of the initial density. This allows the Si IV and Al II lines to remain strongly detected, but the weaker Si II 1808 Å transition is undetected blueward of  $-200$  km s<sup>-1</sup> (Fig. 5). By the time the outflow reaches  $-300$  km s<sup>-1</sup>, the Si IV density is now 1.5 per cent of the original density, and at  $-400$  km s<sup>-1</sup> the density is  $1 \times 10^{-5}$  times the original density. At these densities, the Si IV optical depth drops below the detection threshold, and the line is no longer observed. Meanwhile, the Si II 1260 Å line has an  $f$ -value five times larger and an ionization correction that is twice that of Si IV 1402 Å (see Section 5.2), implying that the Si II  $\tau$  is roughly 10 times larger than the Si IV  $\tau$ . From Fig. 8,

**Table 2.** Parameter estimates to the simultaneous  $\tau$  and  $C_f$  fit of equation (8). Column 2 gives the optical depth normalization ( $\tau_0$ ), column 3 gives the maximum covering fraction ( $C_f(R_i)$ ), column 4 gives the radial velocity-law exponent ( $\beta$ ; equation 7), column 5 gives the density power-law exponent ( $\alpha$ ; equation 5), and column 6 gives the covering fraction exponent ( $\gamma$ ; equation 4). The first row gives the estimates for the high-redshift galaxy J1226+2152, while the second row shows the parameters for the local star-forming galaxy NGC 6090 (Chisholm et al. 2016b).

| Galaxy     | $\tau_0$      | $C_f(R_i)$      | $\beta$         | $\alpha$       | $\gamma$         |
|------------|---------------|-----------------|-----------------|----------------|------------------|
| J1226+2152 | $8.1 \pm 2.5$ | $0.86 \pm 0.03$ | $0.53 \pm 0.10$ | $-6.3 \pm 1.7$ | $-0.53 \pm 0.13$ |
| NGC 6090   | $4.8 \pm 1.4$ | $1.0 \pm 0.04$  | $0.43 \pm 0.07$ | $-5.7 \pm 1.5$ | $-0.82 \pm 0.23$ |

the Si II 1260 Å line is still optically thick at  $-300 \text{ km s}^{-1}$ , with  $\tau$  near 10. Even at large velocities, Si II 1260 Å is optically thick and the profile is determined by  $C_f$ .

Finally, equation (4) explains why  $C_f$  evolves slowly at redder velocities. The rapid acceleration means that the outflow does not travel far in these velocity intervals. At bluer velocities, the outflow covers more distance ( $dv/dr$  is smaller), decreasing the  $C_f$  and shaping the line profiles of the strong lines (Si II 1260 Å, C II 1335 Å, and O VI 1032 Å).

At the moderate spectral resolution of the MEGASaura data, it is important to check that the resolution does not dramatically affect the measured  $C_f$ . To do this, we make a synthetic line profile using the fitted properties from Table 2, and then convolve the profile to the  $75 \text{ km s}^{-1}$  resolution of the MEGASaura data. We then measure the deepest portion of the profile and find that it increases by 0.09 normalized flux units. This increase is within the median  $C_f$  error of 0.13 normalized flux units between  $-400$  and  $0 \text{ km s}^{-1}$  (see Fig. 8), therefore we conclude that the impact of the resolution is within our quoted  $C_f$  errors.

## 5 PHOTOIONIZATION MODELLING

In the previous section, we used the line profiles to show that the O VI column density increases as the Si IV density declines, even though the two phases are co-spatial. This suggests that the O VI column density is decoupled from the Si IV column density, and the low-ionization gas is created by a different mechanism than the transitional gas. In Chisholm et al. (2016a), the low-ionization equivalent widths are consistent with predictions from CLOUDY photoionization models (Ferland et al. 2013), if the observed stellar continuum is the ionizing source. Here, we use the observed column densities and the stellar continuum fit to predict the column densities of the individual transitions. This tests whether the O VI is also photoionized, or if separate ionization mechanisms produce the observed O VI and photoionized gas.

### 5.1 Measuring observed column densities

The observed column density ( $N$ ) of a given transition is the product of the outflow's metallicity, density and ionization structure. To characterize the ionization structure, we measure the integrated column density of each transition using a modified apparent optical depth method (Savage & Sembach 1991) which accounts for non-unity covering of the source (see Section 4.2) as

$$N = \frac{3.77 \times 10^{14} \text{ cm}^{-2}}{\lambda_0 [\text{Å}] f} \int \ln \left( \frac{C_f(R_i)}{C_f(R_i) + F_o(v) - 1} \right) dv, \quad (10)$$

where  $\lambda_0$  is the rest wavelength of each transition,  $f$  is the oscillator strength of each transition and  $F_o(v)$  is the continuum-normalized

flux. We use the  $C_f(R_i)$  from the Si IV 1402 Å transition because many of these lines are singlets, and we cannot derive their velocity-resolved  $C_f$  distributions. Additionally, Chisholm et al. (2016a) show that  $C_f$  does not vary appreciably from transition to transition. This can be seen in Fig. 4 where  $C_f$  appears to be near 0.9 for the strong transitions (where  $C_f = 1 - F$  for saturated lines). The errors are calculated similar to the velocity errors, and a 10 per cent uncertainty is included, in quadrature, to account for the continuum normalization uncertainty. The values are given in Table 1.

Many of these transitions could be heavily saturated. Al III 1862 Å and Si IV 1402 Å are doublets, and their equivalent width ratios diagnose saturation (discussed in Section 3.2). The observed Al III and Si IV doublet ratios are 1.4 and 1.6, respectively, while their  $f$ -value ratios are both 2. This implies that these transitions are not heavily saturated.

The wavelength coverage and sensitivity of the MEGASaura data also allow us to measure lines that are not typically measured (see Pettini et al. 2002, for another example). The Si II 1808 Å line has an  $f$ -value of 0.0025, and is unsaturated. At a signal-to-noise ratio near 10, we marginally detect this line above the continuum noise (a  $3\sigma$  detection; see Fig. 5). The logarithm of the Si II 1808 Å column density is  $15.57 \pm 0.14 \text{ cm}^{-2}$ , which is consistent, within  $2\sigma$ , with the column density measured from Si II 1304 Å and Si II 1526 Å (see Table 1). The photoionization models of the next section rely on the uncertainties of the column densities, and large statistical uncertainties, like the errors we measure for Si II 1808 Å, do not constrain the models. Therefore, we use the Si II 1526 Å column density (as denoted by the 'c' in Table 1), but note that the Si II lines could be marginal saturated.

### 5.2 Can photoionization models reproduce the O VI?

The ionization structure depends on the input energy that heats the gas as well as how efficiently the gas loses energy by radiatively cooling. This cooling depends on the density, temperature, and metallicity of the gas. Consequently, the observed ionization structure sensitively depends on the ionizing spectrum, the density of the outflow, and the metallicity of the outflow.

We characterize the O and B stars ionizing the outflow with the measured STARBURST99 stellar continuum from the wavelength regime redward of 1240 Å. We then model the ionization structure of the outflows using CLOUDY, v13.03 (Ferland et al. 2013), models that use these O and B stars as the ionizing source. In CLOUDY, we use an expanding spherical geometry, with the density profile determined in Section 4.2, and the initial covering fraction ( $C_f(R_i)$ ). By including the fitted density profile from Section 4.2, we incorporate the decreasing outflow density with increasing velocity, which creates the two-regime O VI behaviour (Section 4.1.1). We use CLOUDY's H II abundances, with the Orion nebular dust grain distribution

**Table 3.** CLOUDY parameter grid used to estimate the ionization parameter ( $\log(U)$ ), hydrogen density at the base of the outflow ( $n_{\text{H},0}$ ) and metallicity of the outflow ( $Z_0$ ). The second column gives the parameter range used in the Bayesian analysis and the third column gives the number of bins for each parameter. The expectation values and standard deviations of the parameters for J1226+2152 are given in the fourth column, and the fifth column shows the estimates for NGC 6090, a local star-forming galaxy.

| Parameter<br>(1)       | Range<br>(2)                    | Bins<br>(3) | Expected value<br>(4)       | NGC 6090<br>(5)      |
|------------------------|---------------------------------|-------------|-----------------------------|----------------------|
| $\log(U)$              | $-1.5 \rightarrow -2.5$ dex     | 21          | $-2.01 \pm 0.02$            | $-1.85$              |
| $\log(n_{\text{H},0})$ | $-0.65 \rightarrow 3.2$ dex     | 12          | $42 \pm 31 \text{ cm}^{-3}$ | $19 \text{ cm}^{-3}$ |
| $Z_0$                  | $0.1 \rightarrow 3.0 Z_{\odot}$ | 16          | $1.94 \pm 0.15 Z_{\odot}$   | $1.6 Z_{\odot}$      |

(Baldwin et al. 1991), to account for dust scattering and depletion of metals on to grains. We do not change the relative abundances (like  $\alpha$ -enhancement, or Fe-enrichment), which may have second order effects. We then scale the abundances by constant factors to enrich or deplete the gas according to Table 3. We stop running CLOUDY once the temperature has dropped to 500 K, and include a cosmic ray background (Indriolo et al. 2007).

From a given set of ionization parameters ( $U$ ), outflow metallicities ( $Z_0$ ) and hydrogen densities at the base of the outflow ( $n_{\text{H},0}$ ), CLOUDY estimates the total integrated column densities of the various ions along the line of sight, which we compare to the observed column densities using Bayesian inference (Kauffmann et al. 2003; Brinchmann et al. 2004). We use the large grid of CLOUDY models from Table 3 to calculate the probability of each model, given the observed column densities, using the likelihood function of

$$L \sim \exp(-\chi^2), \quad (11)$$

where  $\chi^2$  is the chi-squared function of the observed O I 1302 Å, Si II 1527 Å, Al II 1670 Å, Al III 1862 Å and Si IV 1402 Å column densities. Note that the observed O VI is not included in these photoionization models because we are trying to predict the O VI column density, given the observed low-ionization column densities, to determine if the observed O VI can be produced by photoionization. We then marginalize over nuisance parameters to produce the probability density functions (PDFs) for each parameter (Fig. 9). We take the expectation values and standard deviations of each of these PDFs as the parameter estimates of  $\log(U)$ ,  $Z_0$  and  $n_{\text{H},0}$  (Table 3).

We then produce a CLOUDY model using the expectation values from the Bayesian inference. This gives the abundances and ionization fractions of each ion. For instance, the CLOUDY model predicts that the neutral fraction of the outflow is 3 per cent, the Si IV ionization fraction is 14 per cent and the gas phase Si/H abundance is  $10^{-5.11 \pm 0.02}$ . The errors on the abundances are calculated by creating CLOUDY models using the standard deviations of the individual parameters. Additionally, the model predicts that the dominant silicon ionization state is Si III (containing 55 per cent of the total silicon), and the outflow has a total hydrogen column density of  $10^{20.75 \pm 0.04} \text{ cm}^{-2}$ . With these photoionization models, and the fitted  $\tau_0$  value, equation (9) solves for the initial radius of the outflow from the ionizing source of  $R_i = 28$  pc. This result is marginally smaller than the 33–101 pc range found for local galaxies in Chisholm et al. (2017).

J1226+2152 has a stellar mass upper limit of  $<10^{9.5} M_{\odot}$  (Wuyts et al. 2012), and the derived  $Z_0$  of  $1.94 \pm 0.15 Z_{\odot}$  is significantly larger than the expected ISM metallicity from the mass–metallicity relation. Local low-mass ( $\sim 10^7 M_{\odot}$ ) dwarf galaxies have similarly enriched galactic outflows, relative to their ISM metallicities

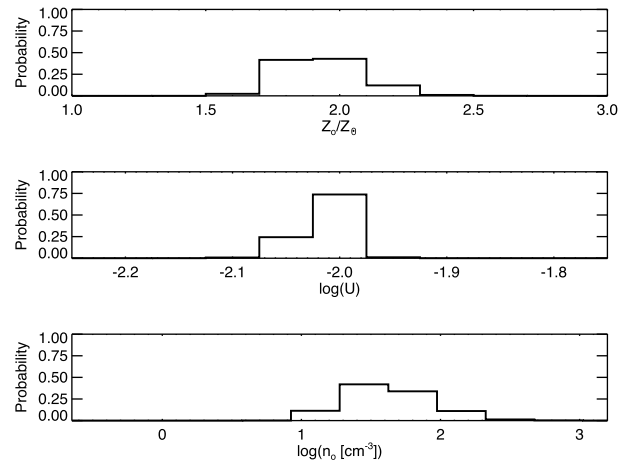


**Figure 9.** Probability density functions for the three parameters used to generate the CLOUDY models: outflow metallicity ( $Z_0$ ), ionization parameter ( $U$ ), and hydrogen density at the base of the outflow ( $n_{\text{H},0}$ ). The expectation values for  $Z_0$ ,  $\log(U)$  and  $n_{\text{H},0}$  are  $1.94 Z_{\odot}$ ,  $-2.01$  dex and  $42 \text{ cm}^{-3}$ , respectively.

(Chisholm et al., in preparation), which is proposed to drive the steep-portion of the observed stellar mass–metallicity relationship because outflows remove a substantial fraction of the metals produced during star formation (Tremonti et al. 2004). Even if the photoionization modelling overestimates  $Z_0$ , the relative results presented below do not change because we adopt the same metallicity for both the photoionized and O VI phases. Further, decreasing  $Z_0$  does not allow for the photoionization models to reproduce the observed O VI column densities.

The fitted CLOUDY column densities have a median deviation of 0.2 dex from the observed values (see the last column of Table 1). The observed Si IV column densities, as well as the lower limits of the blended C IV lines, are consistent with the CLOUDY model, while O VI is not produced at all (see Table 1). Given the observed stellar continuum and the observed low-ion column densities, the CLOUDY models do not produce nearly enough O VI to match the observations. Another ionization mechanism must produce the observed O VI.

## 6 DISCUSSION

### 6.1 How is the O IV created?

Since the photoionization models are unable to create nearly enough O VI, we explore possible alternative mechanisms to produce this transitional gas. The observations provide four constraints:

- (i) O VI has a large integrated column density of  $10^{15.35} \text{ cm}^{-2}$  with velocity-resolved O VI densities near  $2\text{--}10 \times 10^{12} \text{ cm}^{-2} \text{ km}^{-1} \text{ s}$  (Fig. 8).
- (ii) N V is not detected, with upper limits of the N V-to-O VI ratio of  $\log(N(\text{N V})/N(\text{O VI})) < -1.2$  (see Section 3.5 and Fig. 7).
- (iii) C IV and Si IV column densities are consistent with the column densities from the photoionization models, implying that the mechanism that creates the O VI produces negligible Si IV and C IV.
- (iv) Low-ionization lines (like O I, Si II, Al II, etc.) have column densities consistent with the photoionization models.

Below, we explore two excitation mechanisms that satisfy these four constraints. These two mechanisms are not an exhaustive list

of ways to create O VI (see Spitzer 1996; Indebetouw & Shull 2004; Wakker et al. 2012, for reviews), but the above constraints eliminate many other mechanisms. Turbulent mixing layers between hot and cool gas, for example, require a  $\log(N(\text{N v})/N(\text{O vi}))$  near  $-0.5$  (Slavin, Shull & Begelman 1993; Kwak & Shelton 2010), which is inconsistent with constraint (ii) above. Additionally, collisional ionization equilibrium (Sutherland & Dopita 1993), galactic fountain models (Shapiro & Benjamin 1991) and shock models (Allen et al. 2008) do not satisfy constraint (iv) (Chisholm et al. 2016a).

Here, we explore two mechanisms that do satisfy the four criteria above. The two models explain opposite phenomena: cool gas evaporating into a hot medium (Section 6.1.1) and cool gas condensing out of a hot medium (Section 6.1.2). In the next two subsections, we explain the two mechanisms and explore their implications for the ionization fractions of the transitional outflow. We stress that both models have many unconstrained parameters, and rather than trying to derive estimates of the total transitional gas, we maximize the values to predict upper limits. These models must be considered order of magnitude estimates, rather than precise calculations.

### 6.1.1 Conductive evaporation

Thermal conduction transfers thermal energy from a hot ( $>10^7$  K) wind to cooler gas, heating and evaporating the cool gas (McKee & Cowie 1977). As the interaction time increases, conduction heats more of the cool gas. This decreases the total amount of cool gas, while increasing the amount of hot and transitional gas (Indebetouw & Shull 2004). In this case, the O VI is short-lived as the hot outflow further heats the transitional gas to higher temperatures, and the O VI is only observed during this brief transition period.

Many studies explore the evaporation of cool gas by conduction with different assumptions for the direction of the hot flow and the orientation of the magnetic fields (McKee & Cowie 1977; McKee & Ostriker 1977; Ballet, Arnaud & Rothenflug 1986; Borkowski, Balbus & Frstrom 1990; Brüggén & Scannapieco 2016). These studies typically find  $\log(N(\text{N v})/N(\text{O vi}))$  between  $-1.1$  and  $-1.4$ , and  $\log(N(\text{C iv})/N(\text{O vi}))$  between  $-0.4$  and  $-1$  (Indebetouw & Shull 2004). Further, these models predict O VI column densities per velocity interval between  $7$  and  $14 \times 10^{12} \text{ cm}^{-2} \text{ km}^{-1} \text{ s}$ , in agreement with the  $C_f$  corrected column densities observed in Fig. 8. While a different physical situation, conductive interfaces also occur in a supernovae-driven blastwave and produce similar results (Weaver et al. 1977; Slavin et al. 1993; Shelton 1998).

Borkowski et al. (1990) model a time-dependent plane-parallel conductive interface between a hot flow and cooler gas. This model computes the column densities of high-ionization lines like Si IV, C IV, N v and O VI as a function of time, magnetic field orientation, and the physical conditions of the hot wind. In these models, the O VI column density starts with a negligible column density and reaches a saturation level after  $\sim 10^5$  yr, which is similar to the observed  $0.2$  Myr dynamical time of the outflow. Using equation (4) from Borkowski et al. (1990), parameters of the hot wind from Chevalier & Clegg (1985), and assuming that the magnetic field is parallel to the conduction front, we maximize the total hydrogen in the conductive interface, with a value of  $2 \times 10^{19} \text{ cm}^{-2} \text{ km}^{-1} \text{ s}$ . This implies that our observed O VI is  $1 \times 10^{-4}$  times the total hydrogen, and the total integrated hydrogen column density is  $8 \times 10^{21} \text{ cm}^{-2}$  in the conductive interface. Again, these estimations are upper limits because the values are maximized, but these values allow us to compare upper limits of the transitional gas to the photoionized gas in Section 6.2.

**Table 4.** Estimated column densities ( $N$ ; in units of  $\text{cm}^{-2}$ ) of five different ions from the Bordoloi et al. (2017) cooling flow model. These values are estimated using an O VI line width of  $650 \text{ km s}^{-1}$ , an O VI column density of  $10^{15.35} \text{ cm}^{-2}$  and a  $\log(T) = 5.5$  (Bordoloi et al. 2017). This model implies that O VI is 0.8 per cent of the total oxygen.

| Si IV<br>( $\text{cm}^{-2}$ ) | C IV<br>( $\text{cm}^{-2}$ ) | N v<br>( $\text{cm}^{-2}$ ) | O VII<br>( $\text{cm}^{-2}$ ) | O VIII<br>( $\text{cm}^{-2}$ ) |
|-------------------------------|------------------------------|-----------------------------|-------------------------------|--------------------------------|
| $7 \times 10^{13}$            | $5 \times 10^{14}$           | $1 \times 10^{14}$          | $7 \times 10^{16}$            | $2 \times 10^{17}$             |

### 6.1.2 Cooling flow

When hot gas interacts with cool gas, energy flows from the hot gas to the cool gas. If this interaction drops the hot gas temperature to near  $5 \times 10^5$  K, the hot gas radiatively cools and rapidly transitions through temperatures corresponding to O VI.

Recent cooling flow models successfully relate the observed column densities to the line-widths of O VI and N v (Heckman 2002; Bordoloi, Heckman & Norman 2017). These models predict that the total O VI column density increases with the line width, approaching values near  $10^{15} \text{ cm}^{-2}$  for the broadest lines. Using the observed O VI line width of  $650 \text{ km s}^{-1}$  and the column density of  $10^{15.35} \text{ cm}^{-2}$ , the cooling flow model of Bordoloi et al. (2017) predicts the column densities of the other transitions. Table 4 indicates that the  $\log(N(\text{N v})/N(\text{O vi}))$  and  $\log(N(\text{C iv})/N(\text{O vi}))$  ratios are near  $-1.4$  and  $-0.7$ , respectively. Summing up the total oxygen predicted, we find an O VI ionization fraction of 0.8 per cent, a total oxygen column density of  $3 \times 10^{17} \text{ cm}^{-2}$ , and a total hydrogen column density of  $4 \times 10^{20} \text{ cm}^{-2}$ , using the metallicity of the photoionized gas.

## 6.2 Which phase dominates the outflow?

Now that we have explored the creation of the O VI gas, we ask: how does the total transitional phase compare to the photoionized phase? We make this comparison first to the total column densities of the two phases (Section 6.2.1) and then to the mass outflow rates (Section 6.2.2).

### 6.2.1 Comparing the column densities of the two phases

The O I and O VI column densities are ideal to compare because they arise from the same element, and the only difference between the two transitions is their ionization states. O I is an unambiguous tracer of neutral gas because it has the same ionization potential as H I, and the O I ionization fraction is locked to H I through charge exchange. The measured O I column density is  $10^{15.62} \text{ cm}^{-2}$ , nearly a factor of 2 larger than the measured O VI column density. However, at blue velocities the O VI column density likely saturates, and the measured O VI column density could be consistent with the O I column density.

The O I transition only probes neutral gas, which the CLOUDY model suggests is only 3 per cent of the total outflow. The wavelength coverage of the MEGA SAURA data enables us to calculate the total silicon without assuming a model because it contains transitions from each photoionized silicon phase (Si I 1845 Å, Si II 1527 Å, Si III 1206 Å and Si IV 1402 Å; see Table 1). Adding up the observed column densities from these four transitions, we find a lower limit of the total silicon column density of  $10^{15.33} \text{ cm}^{-2}$ , nearly equal to the total O VI column density. The silicon abundance in Section 5.2 provides a total photoionized column density of  $10^{20.5} \text{ cm}^{-2}$ , as compared to the  $10^{21.9}$  and  $10^{20.6} \text{ cm}^{-2}$  found for the conductive



interface and cooling flow models. Summing the observed silicon transitions implies that the total transitional gas has a column density roughly equal to, and at most 20 times larger than, the column density of the photoionized gas.

However, Si III is the dominant ion in the photoionized medium and it is heavily saturated. The CLOUDY model predicts a total hydrogen column density of  $10^{20.75 \pm 0.04} \text{ cm}^{-2}$ . This suggests that the photoionized column density is 2 and 0.1 times the size of the cooling flow and conductive interface models, respectively.

Dust along the line of sight extinguishes the observed stellar continuum. Assuming the dust-to-gas ratio scales with metallicity allows the hydrogen column density to be estimated from the measured extinction (Leitherer et al. 2002; Heckman et al. 2011). Using the relation from Calzetti et al. (2000), the total hydrogen column density is estimated from the UV extinction as

$$N_{\text{H}} = \frac{2.4 \times 10^{21} E_{\text{gas}}(B - V)}{Z}, \quad (12)$$

where  $E_{\text{gas}}(B - V)$  is the gas phase extinction. We convert the measured stellar continuum extinction (0.15 mag) to  $E_{\text{gas}}(B - V)$  by dividing by 0.44 (Calzetti et al. 2000). Using the measured extinction and the derived outflow metallicity, we estimate a total hydrogen column density for the photoionized phase of  $10^{20.64 \pm 0.03} \text{ cm}^{-2}$ , where the uncertainty does not account for the extinction law. The inferred column density from the UV extinction is in agreement, within  $2\sigma$ , with the total hydrogen column density from the CLOUDY models. This inferred photoionized column density is twice as large as the cooling flow column density and one-tenth the conductive interface column density. The exact comparison depends on how the O VI is created and the saturation of O VI. We qualitatively conclude that the photoionized column density is similar to the cooling flow column densities, and smaller than the conductive interface models. The transitional phase gas is a significant portion of the total outflow, and not including the transitional phase would underestimate the total amount of outflowing gas.

### 6.2.2 Comparing the mass outflow rates of the two phases

While deriving column densities does not require assumptions about the outflow geometry, the more fundamental quantity driving galaxy evolution is the mass outflow rate ( $\dot{M}$ ). Here, we calculate  $\dot{M}$  for both the transitional ( $\dot{M}_{\text{tr}}$ ) and photoionized ( $\dot{M}_{\text{ph}}$ ) phases to compare how the phases contribute to the total  $\dot{M}$ .

We calculate  $\dot{M}_{\text{tr}}$  using the observed O VI column density and the photoionized line profile fits. This fitting assumes that the O VI is comoving with the photoionized phase, as suggested by their line profiles (see the discussion in Section 3.2). The O VI mass outflow rate ( $\dot{M}_{\text{O VI}}$ ) is calculated as

$$\dot{M}_{\text{O VI}}(r) = \Omega C_f(r) v(r) m_{\text{O VI}} N_{\text{O VI}}(r) r, \quad (13)$$

where the radial covering fraction (equation 4), velocity law (equation 7) and radius (equation 9) are calculated in Section 3.2 (Table 2). Putting these relations into equation (13) gives  $\dot{M}_{\text{O VI}}$  as

$$\dot{M}_{\text{O VI}}(w) = \Omega C_f(R_i) v_{\infty} m_{\text{O VI}} R_i N_{\text{O VI}}(w) \frac{w}{(1 - w^{1/\beta})^{1+\gamma}}, \quad (14)$$

where  $m_{\text{O VI}}$  is 16 times the proton mass (the mass of oxygen atoms),  $w$  is the velocity normalized by  $v_{\infty}$  (532  $\text{km s}^{-1}$  for O VI), and  $\Omega$  is the solid angle covered by the outflow, which we assume is  $4\pi$ . We use the  $C_f$  corrected O VI column density distribution ( $N_{\text{O VI}}(w)$ ) from Fig. 8. Since the O VI ionization fractions are highly uncertain (see Section 6.1), Fig. 10 shows  $\dot{M}_{\text{O VI}}$  (i.e. only the mass outflow

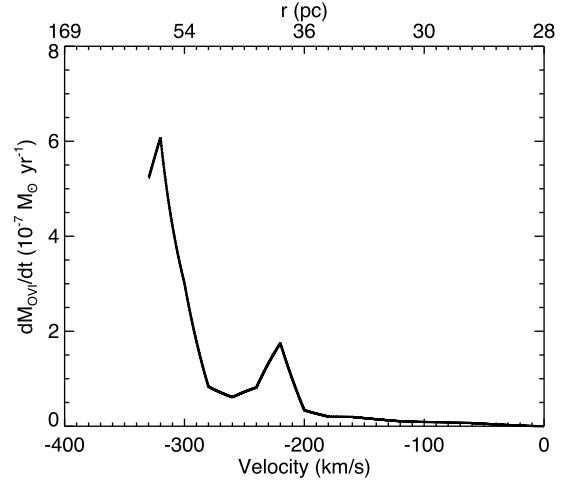


**Figure 10.** The velocity-resolved O VI mass outflow rate ( $dM_{\text{O VI}}/dt$ ) in units of  $10^{-7} M_{\odot} \text{ yr}^{-1}$ . This is calculated assuming that the O VI and Si IV are comoving and co-spatial. The O VI mass outflow rate rises from  $0.2 \pm 0.1 \times 10^{-7} M_{\odot} \text{ yr}^{-1}$  at  $-180 \text{ km s}^{-1}$  to  $6.1 \pm 3.0 \times 10^{-7} M_{\odot} \text{ yr}^{-1}$  at  $-320 \text{ km s}^{-1}$ , increasing by a factor of 30 in  $140 \text{ km s}^{-1}$ . At these velocities, O VI is likely saturated and the O VI mass outflow rate should be considered a lower limit. These are the same velocities that the Al II and Si IV optical depth profiles decline (Figs 6 and 8). The upper x-axis gives the radial distance of the outflow from the ionizing source, using the initial radius and the velocity law (equation 7).

rate of the O VI gas). The  $\dot{M}_{\text{O VI}}$  curve begins at a very low level and steadily increases as the velocity increases. Most of this increase happens between  $-180$  and  $-320 \text{ km s}^{-1}$  where  $\dot{M}_{\text{O VI}}$  increases by a factor of 30. These are the velocities where the O VI profile is likely saturated (see Fig. 6), and  $\dot{M}_{\text{O VI}}$  should be considered a lower limit at these velocities.

Using the ionization corrections found in Section 6.1, we derive upper limits of the total  $\dot{M}_{\text{tr}}$ .  $\dot{M}_{\text{tr}}$  peaks at  $-320 \text{ km s}^{-1}$  with values of  $0.12 M_{\odot} \text{ yr}^{-1}$  and  $0.009 M_{\odot} \text{ yr}^{-1}$  for the conductive interface and cooling flow models, respectively (Fig. 11). These estimates are for the total hydrogen mass outflow rate within the conductive interfaces or cooling flows, but do not include the mass in a hotter phase. It is important to stress that  $\dot{M}_{\text{tr}}$  likely continues rising at the bluest velocities, but the covering fraction corrected O VI column density is not defined past  $-340 \text{ km s}^{-1}$  because the Si IV profile is no longer detected (see Fig. 8).

We follow Chisholm et al. (2016b) and calculate  $\dot{M}_{\text{ph}}$  as

$$\begin{aligned} \dot{M}_{\text{ph}}(r) &= \Omega C_f(r) v(r) \rho(r) r^2 \\ \dot{M}_{\text{ph}}(w) &= \Omega C_f(R_i) v_{\infty} \mu m_p n_{\text{H},0} R_i^2 \frac{w}{(1 - w^{1/\beta})^{2+\gamma+\alpha}}. \end{aligned} \quad (15)$$

Now we use 1.4 times the mass of the proton (the effective mass per nucleon;  $\mu m_p$ ) because we are calculating the total outflowing mass rather than just the O VI mass (we also use this value when calculating  $\dot{M}_{\text{tr}}$  for the conductive interface and cooling flow models above). The parameters are taken from the photoionization modelling and the Si IV profile fitting, where  $v_{\infty}$  is  $-440 \text{ km s}^{-1}$  for the Si IV line.  $n_{\text{H},0}$  in equation (15) is the total hydrogen density from the photoionization modelling in Section 5.2. Importantly, equation (15) has the exact same  $C_f(r)$ ,  $v(r)$  and  $R_i$  as equation (13). The difference between the two relations is the radial density distribution ( $n(r)$  versus  $N_{\text{O VI}}$ ) and the maximum velocity.

The maximum  $\dot{M}_{\text{ph}}$  peaks at  $1.0 \pm 0.4 M_{\odot} \text{ yr}^{-1}$  and decreases at higher and lower velocities, where the  $\dot{M}_{\text{ph}}$  errors are calculated

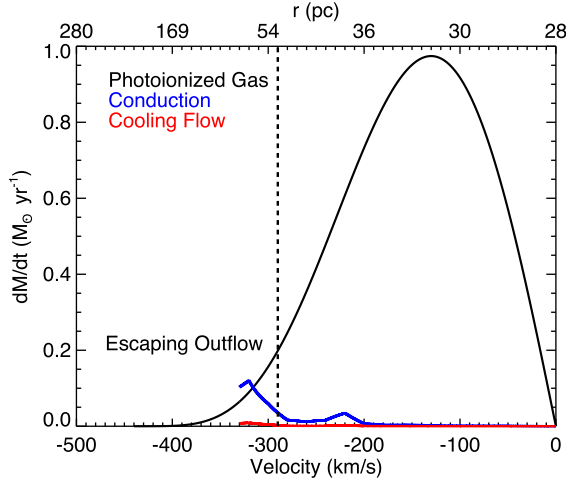


**Figure 11.** The model of the velocity-resolved photoionized mass outflow rate ( $dM/dt$ ; black line), the mass outflow rate from a conductive interface (blue line), and a cooling flow (red line). All of these estimates are for the total hydrogen mass outflow rate in their respective phases. Both the blue and red lines should be treated as upper limits due to uncertain ionization corrections. The photoionized mass outflow rate peaks at  $0.97 \pm 0.39 M_{\odot} \text{ yr}^{-1}$ . The maximum mass outflow rate of the conductive interface model is 12 per cent the peak of the photoionized gas. At  $-290 \text{ km s}^{-1}$ , a dashed line represents the upper limit of the escape velocity for J1226+2152. Any outflow blueward of this velocity is travelling fast enough to escape the gravitational potential of the galaxy. The photoionized outflow rapidly decreases at velocities above the escape velocity, while the transitional mass outflow rate dramatically increases and actually exceeds the photoionized outflow. The upper x-axis gives the radial distance of the outflow from the ionizing source, using the initial radius and the velocity law (equation 7).

using a Monte Carlo analysis of the input parameters from equation (15). The conductive interface  $\dot{M}$  peaks at  $-320 \text{ km s}^{-1}$ , with an upper limit of  $0.12 M_{\odot} \text{ yr}^{-1}$  (blue line in Fig. 11), only 12 per cent of the peak of  $\dot{M}_{\text{ph}}$ . The cooling flow model peaks at the same velocity with an upper limit of  $0.009 M_{\odot} \text{ yr}^{-1}$  (red line in Fig. 11). The photoionized outflow is the chief contributor to  $\dot{M}$  at the observed velocities.

$\dot{M}_{\text{tr}}$  rapidly rises at velocities blueward of  $-200 \text{ km s}^{-1}$ , reminiscent of the velocity that splits the O VI profile into two regimes. The  $\dot{M}_{\text{tr}}$  rises precisely at the same velocity as  $\dot{M}_{\text{ph}}$  declines. In fact, at  $-320 \text{ km s}^{-1}$   $\dot{M}_{\text{tr}}$  exceeds  $\dot{M}_{\text{ph}}$ , indicating that  $\dot{M}_{\text{tr}}$  may dominate at bluer velocities. The continued acceleration of the transitional gas, saturation of the O VI, and the presence of a hotter undetected wind may further increase  $\dot{M}_{\text{tr}}$  and provide the additional  $0.9 M_{\odot} \text{ yr}^{-1}$  required to satisfy mass conservation. These requirements may indicate that the undetected hot wind component dominates the mass outflow rate at higher velocities.

The high-velocity gas is the most important for galaxy evolution because this gas escapes the gravitational potential of the galaxy. Wuyts et al. (2012) place an upper limit on the stellar mass of J1226+2152 at  $\log(M_{*}) < 9.5$ , which leads to an upper limit on the circular velocity of  $< 95 \text{ km s}^{-1}$  (using the Tully–Fischer relation from Reyes et al. 2011). Heckman et al. (2000) approximate the escape velocity as three times the circular velocity, which means that an upper limit for the escape velocity is  $< -290 \text{ km s}^{-1}$ . At these velocities,  $\dot{M}_{\text{ph}}$  rapidly declines while  $\dot{M}_{\text{tr}}$  increases; outflows above the escape velocity may entirely consist of hot and transitional gas. This likely means that studies focusing on cool photoionized gas to calculate the amount of mass escaping galactic potentials

underpredict the total mass of high-velocity outflows. An analysis of the hotter phases are required to accurately determine this quantity.

### 6.3 A physical model explaining these observations

Here, we synthesize the results of the past sections into a physical model that could explain the observations. First, we summarize the observations that our model tries to explain:

(i) The O VI line profile has two regimes, where it matches weak lines at redder velocities and strong lines at bluer velocities (see Figs 4 and 6). Changes in covering fraction drive changes in the line profiles of strong lines, while changes in optical depth drive changes in the line profiles of weak lines. The division line for the O VI profile happens approximately at  $-200 \text{ km s}^{-1}$ .

(ii) The covering fraction corrected Si IV column density drops sharply at bluer velocities (Fig. 8).

(iii) The covering fraction corrected O VI column density is flat at low velocities and increases at high velocities (Fig. 8). The O VI profile transitions from being optical depth dominated at low velocities to covering fraction dominated at high velocities. The O VI column density starts increasing at  $-200 \text{ km s}^{-1}$ .

(iv)  $\dot{M}_{\text{ph}}$  increases at low velocity and decreases at higher velocities as the density and covering fraction decline. As  $\dot{M}_{\text{ph}}$  decreases,  $\dot{M}_{\text{O VI}}$  increases by a factor of 30 (Fig. 10) and actually exceeds  $\dot{M}_{\text{ph}}$  at the highest observed velocities (Fig. 11).

(v) The O VI and photoionized gas are not created by the same mechanism. The CLOUDY models do not reproduce the observed O VI column densities (Table 1), but reasonably reproduce the photoionized gas. The N V non-detection indicates that the O VI is likely produced through conductive evaporation of the photoionized gas or through a cooling flow of a hotter outflow (Section 6.1).

Here, we envision a simple model where a hot ( $> 10^7 \text{ K}$ ) wind is incident on an ensemble of photoionized clouds (see a zoom-in of a single cloud in Fig. 12). The hot outflow accelerates the photoionized clouds from zero-velocity to high velocities by ram pressure, as described by the velocity law in Section 4.2. At the interface of each cloud, heat transfers from the hot outflow to the photoionized clouds through conduction (Weaver et al. 1977), heating the outer layer of photoionized gas to high temperatures. The mass transfer reduces the density of the photoionized gas, while increasing the column density of the O VI and hot wind (lower right panel of Section 4.2). Geometric dilution, elongation from the ram pressure shock, and adiabatic expansion reduce the size and covering fraction of the photoionized clouds (Klein, McKee & Colella 1994; Martin & Bouché 2009; Scannapieco & Brüggén 2015; Brüggén & Scannapieco 2016; Chisholm et al. 2016b). After about 0.2 Myr (the dynamical time of the photoionized clouds), conduction has evaporated most of the photoionized gas and incorporated it into the hot wind (Brüggén & Scannapieco 2016). The process increases the mass of the hot wind, while decreasing its average metallicity, temperature and velocity (Thompson et al. 2016). The transfer of mass from the photoionized phase to the hot wind is often referred to as the mass-loading of the hot wind (Mac Low et al. 1989; Suchkov et al. 1996; Heckman et al. 2000; Strickland & Stevens 2000; Cooper et al. 2009; Strickland & Heckman 2009).

This model explains the observations in a number of ways. First, the O VI is co-spatial with the photoionized gas because the O VI only temporarily arises in the outer layer of the photoionized clouds (see Fig. 12). Second, to satisfy mass conservation, the photoionized mass must directly transfer to the hot wind. Therefore, as the

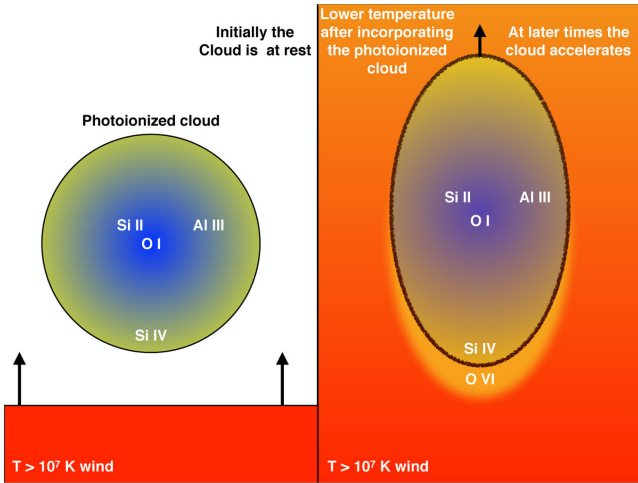


**Figure 12.** Cartoon of the physical picture that produces the O VI absorption. Left-hand Panel: Initial conditions of a photoionized gas cloud at rest. A nearby starburst (not pictured) created a  $T > 10^7$  K wind that propagates towards the photoionized cloud. Hypothetical locations of various observed ions are labelled. Right-hand Panel: A time after the hot wind encountered the photoionized cloud. Ram pressure accelerates and elongates the cloud, while conduction between the hot outflow and the photoionized cloud evaporates the cloud to produce O VI at the interface. Energy from the hot outflow further heats and accelerates the O VI, which reduces the down-stream temperature of the hot wind. By incorporating the photoionized cloud, the down-stream outflow has an increased mass, but a lower temperature, velocity and metallicity.

photoionized density and  $\dot{M}_{\text{ph}}$  decrease,  $\dot{M}_{\text{tr}}$  and  $\dot{M}_{\text{hot}}$  must increase. This indicates that  $\dot{M}_{\text{hot}}$  should be substantial at blue velocities.

Mass-loading of a hot wind with photoionized gas naturally explains the observed two-regime O VI line profile from Section 3.2. Before the hot wind interacts with the photoionized cloud, the cloud is at rest and the photoionized density is large (left-hand panel of Fig. 12). Since photoionization produces negligible O VI, the O VI is optically thin at redder velocities. However, once the hot wind interacts with the photoionized cloud, conduction heats the cloud to temperatures briefly corresponding to O VI (right-hand panel of Fig. 12). As the interaction continues, conduction forges more O VI by heating more photoionized gas. Consequently, while the hot wind accelerates the cloud, the weak low-ionization lines become optically thin as the O VI becomes optically thick. This is precisely what we observe in the lower right panel of Fig. 8. Once O VI saturates, the  $C_f$  of the clouds determines the shape of the profile. This is why the O VI profile closely follows the shape of other saturated lines (Si II and C II). Feeding photoionized gas into a hot wind creates the two-regime O VI line profile because at low velocities conduction has not acted long enough to produce appreciable O VI, while at high velocities conduction has produced enough O VI to saturate the transition.

A prediction of this model is that as the outflow becomes more ionized (and consequently less dense), the velocity must increase to satisfy the continuity equation. The increased velocity causes the mass outflow rate of increasing ionization states to peak at bluer velocities (from photoionized gas to transitional gas in Fig. 11). Chisholm & Matsushita (2016) find that cold molecular outflows have lower outflow velocities than neutral outflows, and this model predicts that, if J1226+2152 has a molecular outflow, the molecular mass outflow rate should peak at velocities redward of  $-130 \text{ km s}^{-1}$ .

### 6.3.1 Does mass-loading of a hot wind impact the CGM?

The small physical distance and the rapid destruction of photoionized clouds means that the observed photoionized clouds do not survive to travel into the circum-galactic medium (CGM). However, cool gas is observed in the CGM around galaxies (Tumlinson et al. 2011; Bordoloi et al. 2014; Werk et al. 2014; Borthakur et al. 2015; Prochaska et al. 2017). Here, we explore reconciling this issue by reforming the warm CGM through a radiative shock of the hot, mass-loaded wind (Wang 1995a,b; Thompson et al. 2016), and the implications that the proposed model of mass-loading has on the formation of the CGM.

At  $1000\text{--}3000 \text{ km s}^{-1}$  (Chevalier & Clegg 1985; Bustard, Zweibel & D’Onghia 2016), the  $T > 10^7$  K hot wind contains most of the outflowing energy. The hot wind travels out of the star-forming region where ambient gas is incorporated into the hot wind. After it is mass-loaded, the hot phase travels outwards with a reduced velocity because the acceleration and heating of the ambient gas consume energy from the hot wind. Gravity, inter-galactic medium pressure, radiative cooling and adiabatic expansion further decrease the velocity and temperature of the hot outflow until it reaches the peak of the cooling curve, which causes the hot outflow to radiatively shock and reform cool photoionized gas (Wang 1995a,b; Thompson et al. 2016).

Changing the initial composition, density, and temperature of the hot wind changes where the hot wind radiatively shocks. Thompson et al. (2016) predict that the cooling radius of the hot wind scales with the mass outflow rate and metallicity of the hot wind as  $\dot{M}_{\text{hot}}^{-2.92}$  and  $Z_{\text{hot}}^{-0.79}$ , respectively. If we assume that the hot wind initially has the mass outflow rate of the transitional gas in Section 6.2.2 (1/8th the photoionized outflow rate) with the metallicity of pure supernovae ejecta ( $\sim 5 Z_{\odot}$ ; Woosley & Weaver 1995), the addition of photoionized mass and metals will increase  $\dot{M}_{\text{hot}}$  but decrease  $Z_{\text{hot}}$ . This increases the cooling radius by a factor of 200 from 10 Mpc scales to 100 kpc scales. Without the mass-loading of cool clouds into the hot wind, the hot wind would not be massive enough to produce the observed metal-enriched CGM within 100 kpc of galaxies (Werk et al. 2014; Prochaska et al. 2017).

Further, whether the hot outflow shocks at all depends on the mass-loading. Thompson et al. (2016) show that there is a minimum ratio between  $\dot{M}$  and SFR – the so-called mass-loading factor – above which the hot wind will radiatively shock. If the mass-loading factor is lower than this minimum mass-loading factor, the hot wind does not lose enough thermal energy to reach the peak of the cooling curve. Therefore, the observed low-ionization CGM gas is never recreated. Thompson et al. (2016) find that the minimum mass-loading factor ranges between  $\dot{M}/\text{SFR} = 0.3$  and 0.6.

Since the mass-loading factor of galactic outflows decreases with increasing stellar mass (Rupke et al. 2005b; Heckman et al. 2015; Chisholm et al. 2017), galaxies greater than  $2\text{--}8 \times 10^{10} M_{\odot}$  generate outflows with mass-loading factors below the minimum mass-loading factor (Chisholm et al. 2017). Hot winds in high-mass galaxies never radiatively shock to produce O VI and low-ionization gas in the CGM. Instead, the temperature of the hot wind remains above the peak of the cooling curve. Tumlinson et al. (2011) detect O VI absorption in 100 per cent of the 19 galaxies with stellar mass less than  $4 \times 10^{10} M_{\odot}$ , but this detection rate drops to 52 per cent for the 23 galaxies with stellar mass greater than  $5 \times 10^{10} M_{\odot}$  (note that these high-mass galaxies contain both star-forming and quiescent galaxies). Similarly, other studies find that the majority of O VI absorption in the CGM arises from galaxies that are fainter than  $L^*$  (Tumlinson & Fang 2005; Stocke et al. 2006; Prochaska et al. 2011b;



Pratt et al. 2017). Since O VI has a cooling time of approximately 1 Myr (Gnat & Sternberg 2007), it acts as a clock for the formation of the CGM. This indicates that the low-ionization gas in the CGM of high-mass galaxies is a relic of an earlier, more mass-loaded, galactic outflow. The mass-loading of a  $10^7$  K wind with cooler photoionized gas may enable the formation of the observed CGM.

## 7 SUMMARY

We searched for O VI in the six galaxies with FUV coverage from MEGASURA. We found O VI in three of the four spectra with signal-to-noise ratios greater than 3 (Fig. 1). We then analysed the interstellar absorption features in the spectrum of SGAS J122651.3+215220 (J1226+2152), a galaxy at a redshift of  $2.926 \pm 0.0002$  that has the highest signal-to-noise ratio near the O VI 1032 Å interstellar absorption line. We used the O VI line, which probes gas transitioning between warm ( $10^4$  K) and hot ( $>10^7$  K) temperatures, to study a seldom-probed phase of galactic outflows. The O VI has an observed column density of  $10^{15.35 \pm 0.05} \text{ cm}^{-2}$  (although it is likely saturated at the bluest velocities) and a maximum outflow velocity near  $-530 \text{ km s}^{-1}$ . The maximum velocity is consistent with saturated low-ionization tracers like C II 1335 Å and Si II 1260 Å (Table 1). We found that the O VI line profile has two regimes: a low-velocity portion that closely resembles weaker low-ionization lines, and a high-velocity portion that resembles the strong saturated lines. The O VI line profile transitions between these two regimes at a velocity of  $-200 \text{ km s}^{-1}$  (Figs 4 and 6). The O VI and photoionized gas have similar velocity profiles and covering fractions, indicating that the two phases are co-spatial.

Using the Si IV doublet, we studied how the optical depth and covering fraction of low-ionization gas vary with velocity. We then corrected the observed Si IV column density for the covering fraction and found that the Si IV column density drops at velocities blueward of  $-200 \text{ km s}^{-1}$ . After correcting the O VI column density for the Si IV covering fraction, the O VI column density rises at velocities blueward of  $-200 \text{ km s}^{-1}$ . O VI is produced as the low-ionization gas is destroyed (Fig. 8).

We used five weak absorption lines to model the ionization structure of the outflow with CLOUDY photoionization models. We found that many of the low-ionization lines are adequately predicted by the photoionization models, but the models produce negligible O VI (see columns 6 and 7 in Table 1). Combined with the non-detection of the N V line (Fig. 7), we postulated that the O VI is created either through conductive evaporation of the photoionized gas by a hot outflow, or through a cooling flow between a hot outflow and the cooler photoionized gas. We used these two models to derive upper limits of the O VI ionization corrections (Section 6.1).

We calculated upper limits of the O VI mass outflow rate and found that it steadily rises at blue velocities (see Fig. 10). The maximum transitional mass outflow rate is at least 10–100 times lower than the maximum of the photoionized mass outflow rate, depending on the O VI ionization mechanism and saturation of O VI. This suggests that the photoionized gas dominates the mass outflow rate at the observed velocities, although the mass outflow rate of the transitional phase rises, and overtakes, the photoionized mass outflow rate at the bluest velocities (Fig. 11).

The O VI phase likely dominates the mass outflow rate at velocities above the escape velocity (Fig. 11). This high-velocity gas completely removes mass from the galaxy, however it is not typically probed by rest-frame UV and optical observations. If studies want to measure the amount of gas removed from galaxies, the hotter outflow phases must be considered.

Finally, we put forth a physical picture where the observed O VI traces the destruction of the photoionized outflow by conduction and the incorporation of the photoionized gas into an unobserved  $>10^7$  K wind (Fig. 12, Section 6.3). To satisfy conservation of mass, the sum of the mass outflow rate for all of the different phases must remain constant, implying that the mass outflow rate of the transitional and hot wind increases as the photoionized mass outflow rate decreases. This is exactly what we observed in Fig. 11. This also implies that the mass outflow rate of the unobserved hot wind is massive and increasing at the largest velocities. We speculated on the effect of incorporating low-ionization gas into a hot wind and the formation of the CGM (Section 6.3.1).

These observations provide new evidence for which gas escapes the gravitational potentials of galaxies. The high-velocity outflow drives the depletion of gas within galaxies, and quantifying it is important to understand what drives the star formation histories of galaxies. Larger samples of rest-frame UV spectra of galaxies with  $z > 2.5$  will constrain the amount of gas removed from galaxies by hot outflows. J1226+2152 is one of the brightest gravitationally lensed galaxies at these redshifts, and it required 12.4 h of integration time on the 6.5 m Magellan telescope. Larger surveys must wait for 20–30 m class telescopes. Furthermore, actually probing the elusive  $10^7$  K wind phase is the largest, and possibly most important, missing component of galactic outflows. Future X-ray observatories, with higher sensitivity and spectral resolution, will measure the hot wind in galaxies outside of the local universe, determining whether hot winds contain the majority of the outflowing mass that escapes galaxies.

## ACKNOWLEDGEMENTS

We thank the referee for a thoughtful read of the paper, and comments that strengthened the work.

Support for this work was provided by NASA through Hubble Fellowship grant #51354 awarded by the Space Telescope Science Institute, which is operated by the Association of Universities for Research in Astronomy, Inc., for NASA, under contract NAS 5-26555.

## REFERENCES

- Allen M. G., Groves B. A., Dopita M. A., Sutherland R. S., Kewley L. J., 2008, *ApJS*, 178, 20
- Arribas S., Colina L., Bellocchi E., Maiolino R., Villar-Martín M., 2014, *A&A*, 568, A14
- Baldwin J. A., Ferland G. J., Martin P. G., Corbin M. R., Cota S. A., Peterson B. M., Slettebak A., 1991, *ApJ*, 374, 580
- Ballet J., Arnaud M., Rothenflug R., 1986, *A&A*, 161, 12
- Bordoloi R. et al., 2014, *ApJ*, 794, 130
- Bordoloi R., Heckman T. M., Norman C. A., 2017, *ApJ*, 848, 122
- Bordoloi R., Rigby J. R., Tumlinson J., Bayliss M. B., Sharon K., Gladders M. G., Wuyts E., 2016b, *MNRAS*, 458, 1891
- Borkowski K. J., Balbus S. A., Fristrom C. C., 1990, *ApJ*, 355, 501
- Borthakur S. et al., 2015, *ApJ*, 813, 46
- Brinchmann J., Charlot S., Heckman T. M., Kauffmann G., Tremonti C., White S. D. M., 2004, preprint ([arXiv:preprint](https://arxiv.org/abs/2004.00000)),
- Brüggen M., Scannapieco E., 2016, *ApJ*, 822, 31
- Bustard C., Zweibel E. G., D’Onghia E., 2016, *ApJ*, 819, 29
- Calzetti D., Armus L., Bohlin R. C., Kinney A. L., Koornneef J., Storchi-Bergmann T., 2000, *ApJ*, 533, 682
- Cardelli J. A., Clayton G. C., Mathis J. S., 1989, *ApJ*, 345, 245
- Chen Y.-M., Tremonti C. A., Heckman T. M., Kauffmann G., Weiner B. J., Brinchmann J., Wang J., 2010, *AJ*, 140, 445
- Chevalier R. A., Clegg A. W., 1985, *Nature*, 317, 44



- Chisholm J., Matsushita S., 2016, *ApJ*, 830, 72
- Chisholm J., Tremonti C. A., Leitherer C., Chen Y., Wofford A., Lundgren B., 2015, *ApJ*, 811, 149
- Chisholm J., Tremonti C. A., Leitherer C., Chen Y., Wofford A., 2016a, *MNRAS*, 457, 3133
- Chisholm J., Tremonti C. A., Leitherer C., Chen Y., 2016b, *MNRAS*, 463, 541
- Chisholm J., Tremonti C. A., Leitherer C., Chen Y., 2017, *MNRAS*, 469, 4831
- Cooper J. L., Bicknell G. V., Sutherland R. S., Bland-Hawthorn J., 2009, *ApJ*, 703, 330
- Ferland G. J. et al., 2013, *RMxAA*, 49, 137
- Fielding D., Quataert E., Martizzi D., Faucher-Giguère C.-A., 2017, *MNRAS*, 470, L39
- Gnat O., Sternberg A., 2007, *ApJS*, 168, 213
- Green G. M. et al., 2015, *ApJ*, 810, 25
- Griffiths R. E., Ptak A., Feigelson E. D., Garmire G., Townsley L., Brandt W. N., Sambruna R., Bregman J. N., 2000, *Science*, 290, 1325
- Grimes J. P., Heckman T., Hoopes C., Strickland D., Aloisi A., Meurer G., Ptak A., 2006, *ApJ*, 648, 310
- Grimes J. P. et al., 2007, *ApJ*, 668, 891
- Grimes J. P. et al., 2009, *ApJS*, 181, 272
- Heckman T. M., 2002, in *Mulchaey J. S., Stocke J. T., eds, ASP Conf. Ser. Vol. 254, Extragalactic Gas at Low Redshift. Astron. Soc. Pac., San Francisco*, p. 292
- Heckman T. M., Armus L., Miley G. K., 1990, *ApJS*, 74, 833
- Heckman T. M., Lehnert M. D., Strickland D. K., Armus L., 2000, *ApJS*, 129, 493
- Heckman T. M., Sembach K. R., Meurer G. R., Strickland D. K., Martin C. L., Calzetti D., Leitherer C., 2001, *ApJ*, 554, 1021
- Heckman T. M. et al., 2011, *ApJ*, 730, 5
- Heckman T. M., Alexandroff R. M., Borthakur S., Overzier R., Leitherer C., 2015, *ApJ*, 809, 147
- Hopkins P. F., Kereš D., Oñorbe J., Faucher-Giguère C.-A., Quataert E., Murray N., Bullock J. S., 2014, *MNRAS*, 445, 581
- Indebetouw R., Shull J. M., 2004, *ApJ*, 605, 205
- Indriolo N., Geballe T. R., Oka T., McCall B. J., 2007, *ApJ*, 671, 1736
- Jenkins E. B., 2009, *ApJ*, 700, 1299
- Kauffmann G. et al., 2003, *MNRAS*, 341, 33
- Klein R. I., McKee C. F., Colella P., 1994, *ApJ*, 420, 213
- Koester B. P., Gladders M. D., Hennawi J. F., Sharon K., Wuyts E., Rigby J. R., Bayliss M. B., Dahle H., 2010, *ApJ*, 723, L73
- Kwak K., Shelton R. L., 2010, *ApJ*, 719, 523
- Lamers H. J. G. L. M., Cassinelli J. P., 1999, *Introduction to Stellar Winds. Cambridge Univ. Press, Cambridge*
- Larson R. B., 1974, *MNRAS*, 169, 229
- Leitherer C. et al., 1999, *ApJS*, 123, 3
- Leitherer C., Li I.-H., Calzetti D., Heckman T. M., 2002, *ApJS*, 140, 303
- Leitherer C., Ortiz O. P. A., Bresolin F., Kudritzki R.-P., Lo Faro B., Pauldrach A. W. A., Pettini M., Rix S. A., 2010, *ApJS*, 189, 309
- Leroy A. K. et al., 2015, *ApJ*, 814, 83
- Mac Low M.-M., McCray R., Norman M. L., 1989, *ApJ*, 337, 141
- Madau P., Pozzetti L., Dickinson M., 1998, *ApJ*, 498, 106
- Markwardt C. B., 2009, in *Bohlender D. A., Durand D., Dowler P., eds, ASP Conf. Ser. Vol. 411, Astronomical Data Analysis Software and Systems XVIII. Astron. Soc. Pac., San Francisco*, p. 251
- Marshall J. L. et al., 2008, in *McLean I. S., Casali M. M., eds, Proc. SPIE Conf. Ser. Vol. 7014, Ground-based and Airborne Instrumentation for Astronomy II. SPIE, Bellingham*, p. 701454
- Martin C. L., 2005, *ApJ*, 621, 227
- Martin C. L., Bouché N., 2009, *ApJ*, 703, 1394
- Matsushita S., Kawabe R., Matsumoto H., Tsuru T. G., Kohno K., Morita K.-I., Okumura S. K., Vila-Vilaró B., 2000, *ApJ*, 545, L107
- McKee C. F., Cowie L. L., 1977, *ApJ*, 215, 213
- McKee C. F., Ostriker J. P., 1977, *ApJ*, 218, 148
- Meynet G., Maeder A., Schaller G., Schaerer D., Charbonnel C., 1994, *A&AS*, 103, 97
- Murray N., Quataert E., Thompson T. A., 2005, *ApJ*, 618, 569
- Murray N., Martin C. L., Quataert E., Thompson T. A., 2007, *ApJ*, 660, 211
- Oppenheimer B. D., Davé R., 2006, *MNRAS*, 373, 1265
- Pettini M., Rix S. A., Steidel C. C., Adelberger K. L., Hunt M. P., Shapley A. E., 2002, *ApJ*, 569, 742
- Pratt C. T., Stocke J. T., Keeney B. A., Danforth C. W., 2017, preprint ([arXiv:1706.05103](https://arxiv.org/abs/1706.05103))
- Prochaska J. X., Kasen D., Rubin K., 2011a, *ApJ*, 734, 24
- Prochaska J. X., Weiner B., Chen H.-W., Mulchaey J., Cooksey K., 2011b, *ApJ*, 740, 91
- Prochaska J. X. et al., 2017, *ApJ*, 837, 169
- Reyes R., Mandelbaum R., Gunn J. E., Pizagno J., Lackner C. N., 2011, *MNRAS*, 417, 2347
- Rigby J. R. et al., 2017a, *ApJ*, in press, preprint ([arXiv:1710.07294](https://arxiv.org/abs/1710.07294))
- Rigby J. R. et al., 2017b, *ApJ*, in press, preprint ([arXiv:1710.07499](https://arxiv.org/abs/1710.07499))
- Rubin K. H. R., Prochaska J. X., Koo D. C., Phillips A. C., Martin C. L., Winstrom L. O., 2014, *ApJ*, 794, 156
- Rupke D. S., Veilleux S., Sanders D. B., 2005a, *ApJS*, 160, 87
- Rupke D. S., Veilleux S., Sanders D. B., 2005b, *ApJS*, 160, 115
- Savage B. D., Sembach K. R., 1991, *ApJ*, 379, 245
- Scannapieco E., Brüggemann M., 2015, *ApJ*, 805, 158
- Scarlata C., Panagia N., 2015, *ApJ*, 801, 43
- Shapiro P. R., Benjamin R. A., 1991, *PASP*, 103, 923
- Sharp R. G., Bland-Hawthorn J., 2010, *ApJ*, 711, 818
- Shelton R. L., 1998, *ApJ*, 504, 785
- Slavin J. D., Shull J. M., Begelman M. C., 1993, *ApJ*, 407, 83
- Sobolev V. V., 1960, *Moving Envelopes of Stars. Harvard Univ. Press, Cambridge*
- Spitzer Jr L., 1956, *ApJ*, 124, 20
- Spitzer Jr L., 1996, *ApJ*, 458, L29
- Springel V., Hernquist L., 2003, *MNRAS*, 339, 312
- Steidel C. C., Erb D. K., Shapley A. E., Pettini M., Reddy N., Bogosavljević M., Rudie G. C., Rakic O., 2010, *ApJ*, 717, 289
- Stocke J. T., Penton S. V., Danforth C. W., Shull J. M., Tumlinson J., McLin K. M., 2006, *ApJ*, 641, 217
- Strickland D. K., Heckman T. M., 2009, *ApJ*, 697, 2030
- Strickland D. K., Stevens I. R., 2000, *MNRAS*, 314, 511
- Suchkov A. A., Berman V. G., Heckman T. M., Balsara D. S., 1996, *ApJ*, 463, 528
- Sutherland R. S., Dopita M. A., 1993, *ApJS*, 88, 253
- Thompson T. A., Quataert E., Zhang D., Weinberg D. H., 2016, *MNRAS*, 455, 1830
- Tremonti C. A. et al., 2004, *ApJ*, 613, 898
- Tumlinson J., Fang T., 2005, *ApJ*, 623, L97
- Tumlinson J. et al., 2011, *Science*, 334, 948
- Veilleux S., Cecil G., Bland-Hawthorn J., 2005, *ARA&A*, 43, 769
- Wakker B. P., Savage B. D., Fox A. J., Benjamin R. A., Shapiro P. R., 2012, *ApJ*, 749, 157
- Walter F. et al., 2017, *ApJ*, 835, 265
- Wang B., 1995a, *ApJ*, 444, 590
- Wang B., 1995b, *ApJ*, 444, L17
- Weaver R., McCray R., Castor J., Shapiro P., Moore R., 1977, *ApJ*, 218, 377
- Weiner B. J. et al., 2009, *ApJ*, 692, 187
- Weiß A., Walter F., Neininger N., Klein U., 1999, *A&A*, 345, L23
- Werk J. K. et al., 2014, *ApJ*, 792, 8
- Westmoquette M. S., Smith L. J., Gallagher J. S., III, Tranco G., Bastian N., Konstantopoulos I. S., 2009, *ApJ*, 696, 192
- White S. D. M., Frenk C. S., 1991, *ApJ*, 379, 52
- Woosley S. E., Weaver T. A., 1995, *ApJS*, 101, 181
- Wuyts E., Rigby J. R., Gladders M. D., Gilbank D. G., Sharon K., Gralla M. B., Bayliss M. B., 2012, *ApJ*, 745, 86

This paper has been typeset from a  $\text{\LaTeX}$  file prepared by the author.